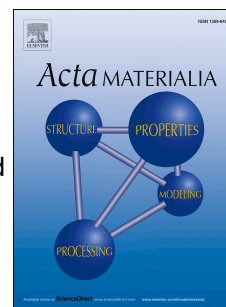


Accepted Manuscript

Mean-field modelling of the intermetallic precipitate phases during heat treatment and additive manufacture of Inconel 718

Magnus J. Anderson, Chinnapat Panwisawas, Yogesh Sovani, Richard P. Turner, Jeffery W. Brooks, Hector C. Basoalto



PII: S1359-6454(18)30526-3

DOI: [10.1016/j.actamat.2018.07.002](https://doi.org/10.1016/j.actamat.2018.07.002)

Reference: AM 14679

To appear in: *Acta Materialia*

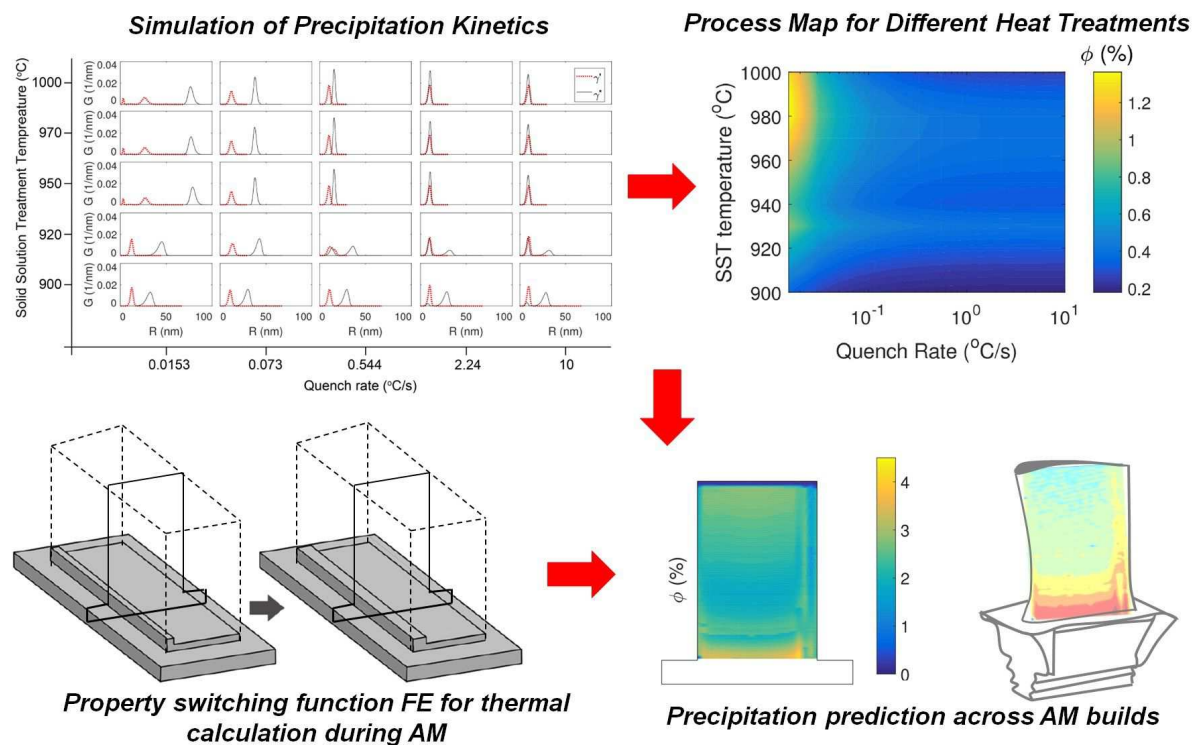
Received Date: 17 April 2018

Revised Date: 18 June 2018

Accepted Date: 1 July 2018

Please cite this article as: M.J. Anderson, C. Panwisawas, Y. Sovani, R.P. Turner, J.W. Brooks, H.C. Basoalto, Mean-field modelling of the intermetallic precipitate phases during heat treatment and additive manufacture of Inconel 718, *Acta Materialia* (2018), doi: 10.1016/j.actamat.2018.07.002.

This is a PDF file of an unedited manuscript that has been accepted for publication. As a service to our customers we are providing this early version of the manuscript. The manuscript will undergo copyediting, typesetting, and review of the resulting proof before it is published in its final form. Please note that during the production process errors may be discovered which could affect the content, and all legal disclaimers that apply to the journal pertain.



Mean-field modelling of the intermetallic precipitate phases during heat treatment and additive manufacture of Inconel 718.

Magnus J. Anderson^a, Chinnapat Panwisawas^{a,b}, Yogesh Sovani^a, Richard P. Turner^a, Jeffery W. Brooks^a, Hector C. Basoalto^a

^a*School of Metallurgy and Materials, University of Birmingham, Edgbaston, Birmingham B15 2TT, UK*

^b*Currently at Department of Materials, University of Oxford, Parks Road, Oxford OX1 3PH, UK*

Abstract

A multi-phase, multi-component mean-field model has been developed for simulating the intermetallic precipitation kinetics in Inconel 718. The aim of this work is to develop predictive capability to aid in process optimisation and explore precipitation kinetics during additive manufacturing (AM). The model has been calibrated to available experimental data, and then applied to predict precipitation kinetics during typical solid solution treatment and aging operations, and during AM. It is shown that a Computer Coupling of Phase Diagrams and Thermochemistry (CALPHAD) based modelling approach provides a unified particle growth rate which can capture the growth, coarsening and dissolution of γ' , γ^* and δ precipitates under relevant heat treatment conditions. To apply the model to AM, finite element simulations of a simple rectangular build have been carried out, using a property switching method to simulate the material deposition. The component level simulation provides the thermal fields to calculate precipitation kinetics during deposition, also allowing for the examination of the heat affected zone in the substrate. The modelling approach can capture the repeated nucleation and dissolution of precipitates that occurs during AM. The model shows good agreement with experimental data when applied to predicting precipitation kinetics during heat treatment.

Keywords: Nickel based superalloy, Inconel 718, precipitation, mean-field

theory, additive manufacture

1. Introduction

Inconel 718 is a precipitate strengthened alloy with three intermetallic dispersed phases; γ' , γ^* and δ . The γ' phase has a face centred cubic ($L1_2$) structure with a stoichiometry of $\text{Ni}_3[\text{Al},\text{Ti}]$. The γ^* phase has a body centred tetragonal (D0_{22}) structure with stoichiometry of $\text{Ni}_3[\text{Nb},\text{Ti},\text{Al}]$ [1]. The δ phase has an orthorhombic structure and shares similar stoichiometry to the γ^* phase. The precipitate strengthening behaviour exhibited by Inconel 718 is attributed to the small, uniformly distributed γ' and γ^* precipitates [2, 3]. The γ' and γ^* nucleate homogeneously whilst δ precipitates nucleate preferentially upon grain boundaries. The δ phase is more thermodynamically stable in comparison to the γ^* phase, and grows at the expense of γ^* particles [4]. Although the δ precipitates do not contribute to the precipitate strengthening behaviour of the alloy, a small amount of δ particles has been suggested to be useful in impeding grain growth during forging and solid solution treatments [5, 3]. Too much δ is undesirable as this depletes the Nb content from the matrix, reducing the amount of γ^* that can form [6, 7]. The morphology of the precipitate phases differ, with globular γ' precipitates, disc shaped γ^* and plate like δ particles [8].

Conventional programmes aimed at designing heat treatments or assessing thermal stability of precipitates under conditions relevant to component service require expensive, time consuming material characterisation. A simulation tool is needed that better captures the precipitation behaviour under such conditions, allowing for the fast screening of potential heat treatments and the calculation of particle coarsening during component service. Furthermore, the calculation of statistical information regarding the precipitate phase distributions may be used in the determination of mechanical properties [9, 10]. The ability to predict the nucleation, growth and coarsening of these precipitates during processing and service is an essential part of an integrated computational materials engineering (ICME) framework that exploits microstructure-property relationships for the

identification of optimum process conditions.

The rate at which γ' , γ^* and δ precipitates nucleate and grow is controlled by the diffusion of the particle forming species within the matrix. This may be modelled explicitly using Kinetic Monte Carlo [11, 12]. These methods calculate the atomic jump frequency as a function of the atomic arrangement, allowing for the prediction of ordered phases. This approach requires the identification and characterisation of the different diffusion pathways, accounting for all possible spatial configurations of the alloying elements. As the number of alloying elements is increased, a greater number of diffusion mechanisms operate, increasing the number of atomic configurations that must be assessed. Consequently, this approach becomes computationally expensive and complex when considering multi-component alloys such as the typical engineering nickel-based superalloys used in turbine engines.

A continuum description of the diffusion fields becomes advantageous when describing the kinetics of such particles. Phase field or sharp interface models offer the ability to capture the interaction of neighbouring particles where overlapping diffusion fields and elastic stresses affect the particle morphology and growth rate [4, 13, 14]. Such approaches have been successful in the development of the understanding of the physical mechanisms responsible for the observed behaviour. However, it remains a challenge to simulate a significant number of particles during the entire heat treatment process so that the results are of statistical significance and may be applied to predicting macro-scale properties. For example, in the phase field approach of Zhou *et al.* [4], the δ precipitates grew to reach both boundaries of the simulation domain, becoming infinitely long.

When dealing with large number of particles, mean-field descriptions have proven useful in the reduction of the many-body problem to a one-particle problem. This involves approximating the precipitate morphology by simple geometry and using mean values to describe the chemical concentration within the particle, matrix and at the particle-matrix interface. Such frameworks are based on solving a continuity statement on the particle size distribution. Fundamen-

tal to solving the continuity condition is knowledge of an appropriate particle growth rate. Lifshitz and Slyozov [15] and Wagner [16] (LSW) developed the first complete mean-field description of Ostwald ripening, which has been extended to include nucleation using classical nucleation theory [17, 18, 19]. LSW described the kinetics of a dilute dispersion of particles within a binary alloy. Several authors have further developed this work to apply to multicomponent alloys [20, 18, 21]. Mean-field theory assumes weak interaction between precipitates. Correction factors are often introduced to capture the accelerated coarsening kinetics as the volume fraction of precipitates increases due to the overlapping of diffusion fields [22, 23, 24, 25]. Svoboda *et al.* [18] include the impact of misfit strain within the calculation of the particle growth rate but do not account for interaction between neighbouring precipitates distortion of the matrix. Another consideration is particle coalescence [26], which may be included within a mean-field framework and can be important when considering precipitation kinetics in high volume fraction particle dispersions.

Fisk *et al.* [9] have developed a mean-field model that predicts the nucleation, growth and coarsening of γ^* precipitates within Inconel 718. They treated the classical regimes of nucleation, growth and coarsening separately, using different expressions to describe the growth rate of nuclei or particles during these regimes. The multi-component mean-field description developed by Svoboda *et al.* [18] can capture these regimes within a unified model, calculating the kinetics of multiple precipitate phases. This model is referred to as the Svoboda-Fischer-Fratzl-Kozeschnik (SFFK) model. Zickler *et al.* [27] have applied the SFFK model to simulate the precipitation kinetics of the γ' and δ phases in the Nickel based superalloy Allvac 718Plus. Moore *et al.* [28] have built upon the SFFK model, utilising the shape factors of Kozeschnik *et al.* [29] and aspect ratio kinetics of Svoboda *et al.* [30] to capture the evolution of disc-shaped γ^* precipitates within the Ni-based Alloy 625. The model presented in this work combines these approaches to simulate the precipitation kinetics of γ', γ^* and δ in Inconel 718 using Kozeschnik *et al.*'s [29] shape factors to approximate the γ^* and δ as cylinders.

Many authors [1, 2, 3, 31, 32] have reported aspects of the precipitation kinetics of the γ' , γ^* and δ phases in Inconel 718. Azadian *et al.* [2] and Beaubois *et al.* [3] provide isothermal aging behaviour of δ precipitates, whilst Fisk *et al.* [1] has summarised and added to isothermal aging data regarding the coarsening kinetics of γ^* during isothermal aging. MaiWald-Immer and Fischersworring-Bun [31] provide measurements of γ^* and γ' during isothermal aging and as a result of a solid solution treatment and two-step age. This data has been used to calibrate model parameters. The second problem is the application of the mean-field model to the simulation of precipitation kinetics during standard heat treatments, generating a process map to assist in the design and optimisation of the heat treatment. The model has then been applied to predict precipitation kinetics during powder-bed fusion AM. The build design and laser path used to form the components results in a complex thermal history. The thermal gradients generated within the component result in residual stress and distortion which may be mitigated when designing the laser path, and then compensated for when designing the component geometry. Another key consideration is the variation in microstructure developed in an additive manufactured component. The temperature history on a particular build will dictate and drive the microstructural development, e.g. process-induced porosity, grain size distribution and precipitation. To understand and optimise the mechanical properties of components made out of nickel-based superalloys, it is necessary to control the precipitation kinetics of intermetallic particles. One concern is that the strengthening precipitates may nucleate during AM to such an extent as to affect mechanical properties and thus residual stresses. Tucho *et al.* [33] have measured differences of up to 10% in hardness across a build and attribute this to the location specific precipitation of γ' and γ^* that forms during deposition. Another issue is that the thermal loading applied during AM may result in the nucleation of an excessive amount of the δ phase as observed by Idell *et al.* [34] in a similar alloy (ATI 718Plus).

The precipitation model has been developed to address these issues, and has been applied to simulate the kinetics at a cross section of an AM component. A

finite element simulation has been used to determine the thermal history that is input into the precipitation model. The simulation tool has been used to investigate the precipitation kinetics during AM and to assess the heat-affected zone within the substrate.

In brief, the aim of this work is to present the developed multi-phase, multi-component mean-field model and illustrate how the SFFK particle growth rate with shape factors can capture the precipitation kinetics of all intermetallic phases in Inconel 718. The applicability of the model is tested by applying the model to predict kinetics during heat treatments and during AM. The results show that the model assumptions are suitable when applied to conventional heat treatments, however the heterogeneity in local chemistry that develop during AM is the likely cause for differences in predicted precipitation kinetics and experimental data. The following section presents the model formulations for precipitation kinetics and the AM process. The next section outlines the model parameters, and calibration. Section 4 presents the predicted process maps for heat treatment and the results when applied to modelling precipitation during AM. The findings are discussed and concluded in Section 5.

2. Model Formulation

2.1. Precipitation kinetics

In this modelling approach, the particles are treated as either spherical or cylindrical with their growth rate a function of the particle size, the composition of the matrix and that of the precipitate phases. The particle dispersion is described by the distribution function $F(R,t)dR$, which is the number of particles of size varying between R and $R + dR$ within a representative volume V , at a given time, t . Statistical information of interest regarding the particle

dispersion is calculated from moments of $F(R, t)$ with respect to R ,

$$\begin{aligned} N_v(t) &= \frac{1}{V} \int_0^\infty F(R, t) dR \\ \langle R(t) \rangle &= \int_0^\infty RF(R, t) dR / \int_0^\infty F(R, t) dR \\ \phi(t) &= \frac{4\pi}{3V} \int_0^\infty R^3 F(R, t) dR \end{aligned} \quad (1)$$

where $N_v(t)$ is the particle concentration, $\langle R(t) \rangle$ is the mean particle radius, and $\phi(t)$ is the particle volume fraction. The evolution of the particle distribution is determined by solving the continuity equation,

$$\frac{\partial F(R, t)}{\partial t} + \frac{\partial F(R, t)V(R, t)}{\partial R} = I(R, t) \quad (2)$$

where the particle growth rate is given by $V(R, t)$ and the nucleation rate by $I(R, t)$. The generalised particle growth rate descriptive of Ostwald ripening kinetics is,

$$V(R, t) = \frac{A(t)}{R} \left(\frac{1}{R_c(t)} - \frac{1}{R} \right) z(R, t) \quad (3)$$

where the term $A(t)$ includes the rate of diffusion of alloying elements at the particle-matrix interface. $R_c(t)$ is the critical particle radius, with particles smaller than this value dissolving and those larger growing. The term $z(R, t)$ accounts for the impact of the overlap of diffusion fields between neighbouring particles, accelerating particle growth kinetics. Marqusee and Ross [22] derived the following correction factor,

$$z(R, t) = 1 + R\sqrt{4\pi N_v(t)\langle R(t) \rangle} \quad (4)$$

The multi-component SFFK particle growth rate has been applied in this work. The parameters for the growth rate given in Equation 3 using the SFFK model are listed below,

$$A(t) = \frac{2\sigma}{R_g T} \left[\sum_{i=1}^n \frac{(c_{ki} - c_{0i})^2}{c_{0i} D_{0i}} \right]^{-1} \quad (5)$$

$$R_c(t) = \frac{2\sigma}{\Delta G_c} \quad (6)$$

where c_{ki} and c_{0i} describe the molar concentrations of the i th alloying element in the particle and matrix phases, respectively. R_g and T are the gas constant and the absolute temperature. The diffusivity of the i th alloying element within the matrix is given by D_{0i} . The interfacial energy is given by σ .

The term ΔG_c in Equation 6 is the chemical driving force,

$$\Delta G_c = -U - \sum_{i=1}^n c_{ki} (\mu_{ki} - \mu_{0i}) \quad (7)$$

The terms μ_{ki} and μ_{0i} refer to the chemical potentials of the precipitate and matrix phases considering the i th alloying element. The misfit strain energy is given by U .

The γ^* and δ phases are approximated by cylinders using the shape factors of Kozeschnik *et al.* [29]. The cylinder is defined by the aspect ratio, $h = H/D$, where H refers to the height of the cylinder, and D its diameter. The shape factors S_k and O_k are introduced into the particle growth rate as follows,

$$A(t) = \frac{2\sigma S_k}{R_g T O_k} \left[\sum_{i=1}^n \frac{(c_{ki} - c_{0i})^2}{c_{0i} D_{0i}} \right]^{-1} \quad (8)$$

$$R_c(t) = \frac{2\sigma S_k}{-\sum_{i=1}^n c_{ki} (\mu_{ki} - \mu_{0i})} \quad (9)$$

where the shape factors are functions of the aspect ratio [29, 30],

$$S_k = 0.2912h^{2/3} + 0.5824h^{-1/3} \quad (10)$$

$$O_k = 0.881h^{-0.122} \quad (11)$$

Nucleation is treated classically, with the transient nucleation rate given by [35],

$$I_s = Z\beta^* N_c \exp\left(\frac{-\Delta G^*}{k_b T}\right) \quad (12)$$

$$I = I_s \exp\left(\frac{-\tau}{t}\right)$$

where the Z term refers to the Zeldovitch factor, β^* is the atomic attachment rate, N_c is the number density concentration of nuclei, and ΔG^* is the nucleation

barrier. The Boltzmann constant is given by k_b . The incubation time is given by,

$$\tau = \frac{1}{2\beta^* Z^2} \quad (13)$$

The expression used in this work to define the Zeldovitch parameter is given below [17],

$$Z = \sqrt{\frac{\Omega^2 \sigma}{4\pi^2 k_B T R_c^4}} \quad (14)$$

where Ω is the atomic volume.

The energy barrier to nuclei formation is given by,

$$\Delta G^* = \frac{1}{\psi^3} \frac{16\pi}{3} \frac{\sigma^3}{(\Delta G_c)^2} \quad (15)$$

where ψ is the sphericity of the nuclei given by Equation 16.

$$\psi = \frac{(6\sqrt{\pi} V_p)^{2/3}}{A_p} \quad (16)$$

where V_p and A_p refer to the particle volume and surface area, respectively. The relationship between sphericity and the aspect ratio h of a cylinder is given by,

$$\psi = \left(h + \frac{1}{2}\right)^{-1} \left(\frac{3}{2}h\right)^{2/3} \quad (17)$$

Svoboda *et al.* [18] derived the following multi-component approximation for the atomic attachment rate in a multi-component alloy,

$$\beta^* = \frac{4\pi R_c^2}{a^4 \bar{V}_m} \left(\sum_{i=1}^n \frac{(c_{ki} - c_{0i})^2}{c_{0i} D_{0i}} \right)^{-1} \quad (18)$$

where \bar{V}_m is the molar volume, and a is the lattice parameter. Similar to the observation of Bonvalet *et al.* [36], the description of the critical nuclei radius is equivalent to that of the critical particle radius given in Equation 6.

Jou *et al.* [17] provide the following Gaussian waveform to approximate the nuclei concentration density,

$$N_c = \frac{N_0}{\Delta R \sqrt{2\pi}} \exp\left(-\frac{(R - R_c)^2}{2(\Delta R)^2}\right) \quad (19)$$

where N_0 is the concentration of nuclei sites and ΔR is the variance of the nuclei size distribution. An expression for ΔR may be obtained from the Zeldovitch parameter. The Zeldovitch parameter is descriptive of the gradient of $\partial G/\partial R$ at $R = R_c$ [35]. ΔR is approximated as the width of plus or minus a thermal fluctuation $k_b T$ from R_c ,

$$\Delta R = \left(\frac{3\Omega}{2(\pi)^{3/2}} \frac{1}{Z} \right)^{\frac{1}{3}} \quad (20)$$

where Ω is the atomic volume. The number concentration of nuclei, N_0 is approximated by considering the supersaturation and the mean size of stable nuclei (R_c),

$$N_0 = \eta \frac{3(\phi_{eq} - \phi(t))\omega}{4\pi R_c^3} \quad (21)$$

where ϕ_{eq} is the equilibrium volume fraction and ω is the unit volume containing the particle dispersion. The parameter η describes the fraction of active nucleation sites. For homogenous nucleation, η is given by unity. For heterogeneous nucleation at grain boundaries, η is determined by the fraction of nucleation sites found on grain boundaries.

To describe nucleation during a complex thermal cycle, an incubation probability P_{inc} is introduced so that the transient nucleation rate is given by $I = I_s P_{inc}$. The incubation probability describes the likelihood that stable nuclei have formed. P_{inc} is defined as the ratio of the current nuclei concentration divided by the steady state nuclei concentration. The definitions of the transient and steady state nucleation rates given in Equation set 12 give the incubation probability as

$$P_{inc} = \exp\left(\frac{-\tau}{t}\right) \quad (22)$$

P_{inc} may be numerically integrated during the calculation. If Equations 18 and 14 are substituted into Equation 13, the following description of the incubation time is obtained,

$$\tau = \frac{k_B T R_c^2}{2\theta \sigma a^2} \quad (23)$$

where θ contains the diffusivity terms,

$$\theta = \left[\sum_{i=1}^n \frac{X_{ki} - X_{0i}}{X_{0i} D_{0i}} \right]^{-1} \quad (24)$$

The incubation probability is thus given by,

$$P_{\text{inc}}(t, T, \theta, R_c, \sigma) = \exp\left(\frac{-\tau}{t}\right) = \exp\left(-\frac{1}{t} \frac{2\theta\sigma a^2}{k_B T R_c^2}\right) \quad (25)$$

To describe non-isothermal conditions an equivalent time is introduced. The equivalent time, t_{eq} , is obtained by rearranging the incubation probability for time,

$$t_{eq} = -\frac{\tau}{\ln(P_{\text{inc}})} \quad (26)$$

where $0 < P_{\text{inc}} < 1$. The temporal derivative of Equation 25 is shown below,

$$\frac{dP_{\text{inc}}}{dt} = \frac{\partial P_{\text{inc}}}{\partial t} + \frac{\partial P_{\text{inc}}}{\partial T} \frac{dT}{dt} + \frac{\partial P_{\text{inc}}}{\partial \theta} \frac{d\theta}{dt} + \frac{\partial P_{\text{inc}}}{\partial R_c} \frac{dR_c}{dt} + \frac{\partial P_{\text{inc}}}{\partial \sigma} \frac{d\sigma}{dt} \quad (27)$$

Making use of the chain rule, the derivative of the incubation probability can be expressed as follows,

$$\frac{dP_{\text{inc}}}{dt} = \frac{\tau}{t_{eq}} P_{\text{inc}} \left[\frac{1}{t_{eq}} + \left(\frac{1}{\theta} \frac{d\theta}{dT} - \frac{2}{R_c} \frac{dR_c}{dT} + \frac{1}{\sigma} \frac{d\sigma}{dT} - 1 \right) \frac{dT}{dt} \right] \quad (28)$$

2.2. Additive manufacture model

Finite element analysis has been used to simulate the AM process, calculating the component geometry and thermal history using the approach described by Mukherjee *et al.* [37]. The melting and solidification of the powder particles is modelled using the ‘property switching element (PSE)’ method. This involves discretising the domain using finite elements into regions with the properties assigned to either a gas or the metallic phase. Initially, the deposition domain has gas properties whilst the substrate is assigned the thermo-physical and elastic properties of Inconel 718. After the introduction of a volumetric heat source, the corresponding deposition domain attached within the heat source is switched to Inconel 718 materials properties. The algorithm proceeds successively until the final fabrication layer is reached, replicating the AM process. Likewise, the

thermal model is treated by heat transfer calculations based upon metallic or air properties on the deposited elements.

The heat source descriptive of the laser is modelled using surface and volumetric heat sources. The surface heat source at a position given by the coordinates $[x, y]$ is given by,

$$Q_s(x, y) = \frac{D\eta P}{\pi R_b^2} \exp\left(-\frac{D(x^2 + y^2)}{R_b^2}\right) \quad (29)$$

where D is the beam distribution parameter, η is the absorption coefficient, P is the laser power, and R_b is the laser beam radius. The volumetric source rate, $Q_v(x, y, z)$ is given by,

$$Q_v(x, y, z) = \frac{D\eta P}{\pi R_b^2 L_H} \exp\left(-\frac{D(x^2 + y^2 + z^2)}{R_b^2}\right) \quad (30)$$

where L_H is the layer height. The heat source moves at a the velocity, v .

The assumptions made in this calculation are: (i) conductivity, specific heat and density are isotropic, (ii) a larger layer height is simulated in comparison to the powder size, with the entire layer in the entire element fabricated at the same time instance as the scanning speed is fast and the simulation of the actual layer dimensions is computationally expensive, (iii) the heat source distribution is considered to be uniform across the deposition layer, and (iv) the convective heat transfer is assumed to be spatially independent.

3. Solution implementation

3.1. Mean-field modelling

The multi-component precipitation model requires a thermodynamic and mobility database to provide information regarding particle compositions, chemical potentials, and diffusivities. This work utilises the TTNi8 thermodynamic database with the MOBNi1 mobility database, using the TQ FORTRAN interface in the commercial software ThermoCalc [38]. As the γ^* phase is metastable, it is necessary to suspend the more thermodynamically favourable δ phase to

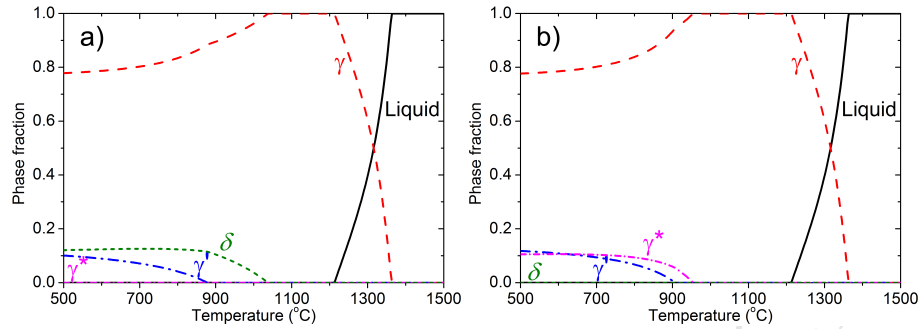


Figure 1: The simulated phase diagram of Inconel 718. Figure a) includes the γ , γ' , γ^* , δ and liquid phases. In Figure b) the δ phase is suspended, allowing for the prediction of stable γ^* .

assess the composition and chemical potential of the γ^* . This is illustrated in Figure 1, which shows simulated phase diagrams considering γ , liquid and intermetallic precipitates phases. In Figure 1 (a), a large equilibrium volume fraction of δ is predicted, with no γ^* .

The thermodynamic database has been calibrated to better describe the solvus temperature of the γ^* and δ phases using the solvus temperatures provided by de Jaeger *et al.* [39]. Energy contributions have been applied to these phases to achieve solvus temperatures of 940°C and 1025°C for the γ^* and δ phases, respectively.

It is assumed that during AM solidification occurs quickly, and does not significantly affect subsequent precipitation. The thermal fields predicted by the FEA simulation suggests that remelting is likely to occur during the build. To account for this behaviour, incipient melting has been included. The liquidation temperature of the intermetallic phases has been calculated using the thermodynamic database. If the temperature exceeds the liquidation temperature of the intermetallic phase, the precipitates are removed from the calculation.

The evolution of the particle dispersions has been calculated by solving the continuity equation shown in Equation 2 using the numerical methods described by Anderson *et al.* [40]. The gradients $d\theta/dT$, dR_c/dT and $d\sigma/dT$ shown in Equation 28 are calculated numerically. The equilibrium composition and chem-

ical potential of the γ' , γ^* and δ phases were calculated as a function of temperature prior to precipitation calculations. This information was interpolated for the specific temperatures of interest. The chemical potential and diffusivities of elements within the γ phase were calculated during the precipitation simulation.

The interfacial energy of each precipitate phase has been assumed to be temperature dependent, and has been treated as a calibration parameter to fit the precipitate measurements presented by Azadian *et al.* [2], MaiWald-Immer and Fischersworing-Bun [31] and those collated by Fisk *et al.* [1]. This was achieved through an iterative process consisting of first calibrating the δ phase, and then ensuring that the γ^* is still stable, and coarsens correctly. The γ' phase was calibrated last, as this phase was found to be less sensitive to the presence of the other phases. The calibration obtained in this work is presented in Figure 2. We predict the formation of delta at 760°C, which was also observed by Slama *et al.* [41].

Figure 3 shows the ability to simulate the size and volume fraction of the δ phase. Figure 3 b), d), f) and g) compare the predicted evolution of the volume fraction of δ with measurements. The predicted volume fraction of δ at 900°C is lower than measured, and is due to differences between the predicted equilibrium phase diagram for the δ phase and the measured values. The thermodynamic database predicts a maximum of approximately 12% δ as shown in Figure 1 whilst Azadian *et al.* [2] have measured area fractions as high as 18%. The calibration successfully captures the mean height of δ particles at temperatures of 1000°C and 950°C however over predicts the size of the particles at 900°C and 850°C. This discrepancy was accepted, as the formation of the δ phase is of most interest at high temperatures and the calibration captures the correct trends in the increase of the volume fraction towards the equilibrium volume fraction of the δ phase. Capturing the volume fraction of δ is more important, as it allows for the determination of correct matrix chemistries used to calculate the kinetics of γ^* . The difficulty in accurately capturing the low temperature δ kinetics may be due to nucleation of intra-granular δ at lower temperature [42] or changes in the aspect ratio of the δ precipitates.

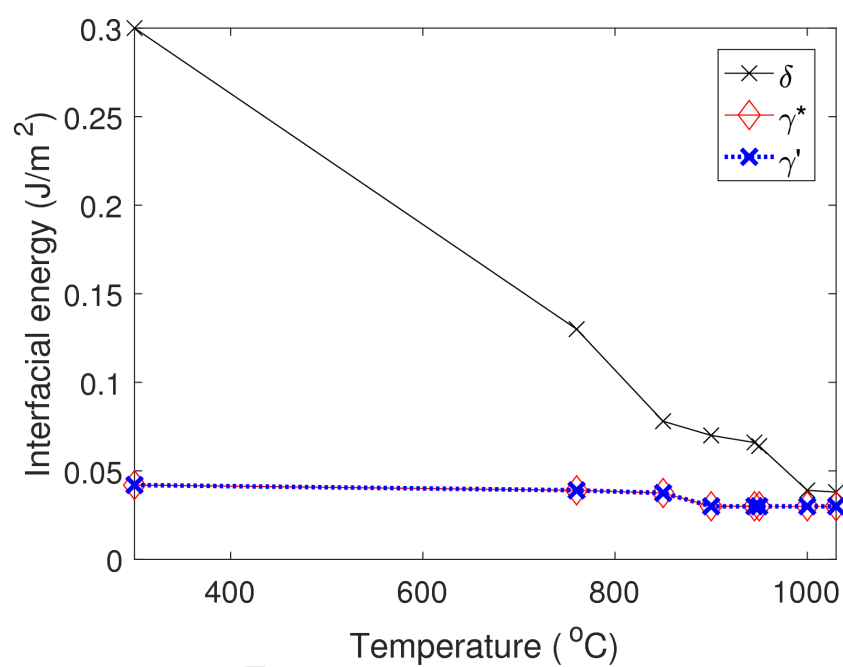


Figure 2: The calibrated interfacial energy as a function of temperature for the δ , γ^* and γ' phases.

Figure 4 compares the simulated nucleation, growth and coarsening kinetics of the γ^* phase during isothermal aging at 760°C with the measurements collated by Fisk *et al.* [1].

Figure 5 compares the predicted size and volume fraction of γ' and γ^* against the measurements of Brooks and Bridges [32] and MaiWald-Immer and Fischersworring-Bunk [31]. The error bars in Figures a) and e) refer to the first and third quartiles. The error bars in Figure b) were obtained from quantifying the uncertainty in the TEM foil thickness and measuring precipitate area fractions from the TEM micrographs. The model captures MaiWald-Immer and Fischersworring-Bunk [31]'s data with reasonable accuracy. The model overpredicts the increase in volume fraction during aging at 700°C as shown in Figure 5 f) however captures the size evolution adequately (Figure 5 e)). Figure 5 b) shows the volume fraction increase and then fall over time during aging at 800°C. The model predicts similar behaviour, with the decrease in volume fraction caused by the formation of δ precipitates.

3.2. Additive Manufacture

In order to replicate the thermal history during the AM process, a thermal model using finite element methods has been applied using Abaqus/Standard 6.13.1. Three user materials subroutines have been written to: (i) alter the element property between air and the metallic phases using the 'property switching elements' method, (ii) apply the thermal load for each deposition layer, and (iii) the calculation of convective heat transfer using Inconel 718 thermal physical properties. The AM simulation utilises the Inconel 718 thermal physical properties of Song *et al.* [43] and Raghavan *et al.* [44].

The 8-node linear brick element type is used for heat transfer calculations. The substrate is a cuboid with dimension of 100mm \times 32mm \times 5mm. The deposition geometry is also cuboidal, with dimensions of 80mm \times 20 mm \times 30mm, as illustrated in Figure 6 a). The AM process is simulated by modelling the sequential addition of lines of material with dimensions of 80mm \times 1mm \times 0.3mm, as shown in Figure 6 b).

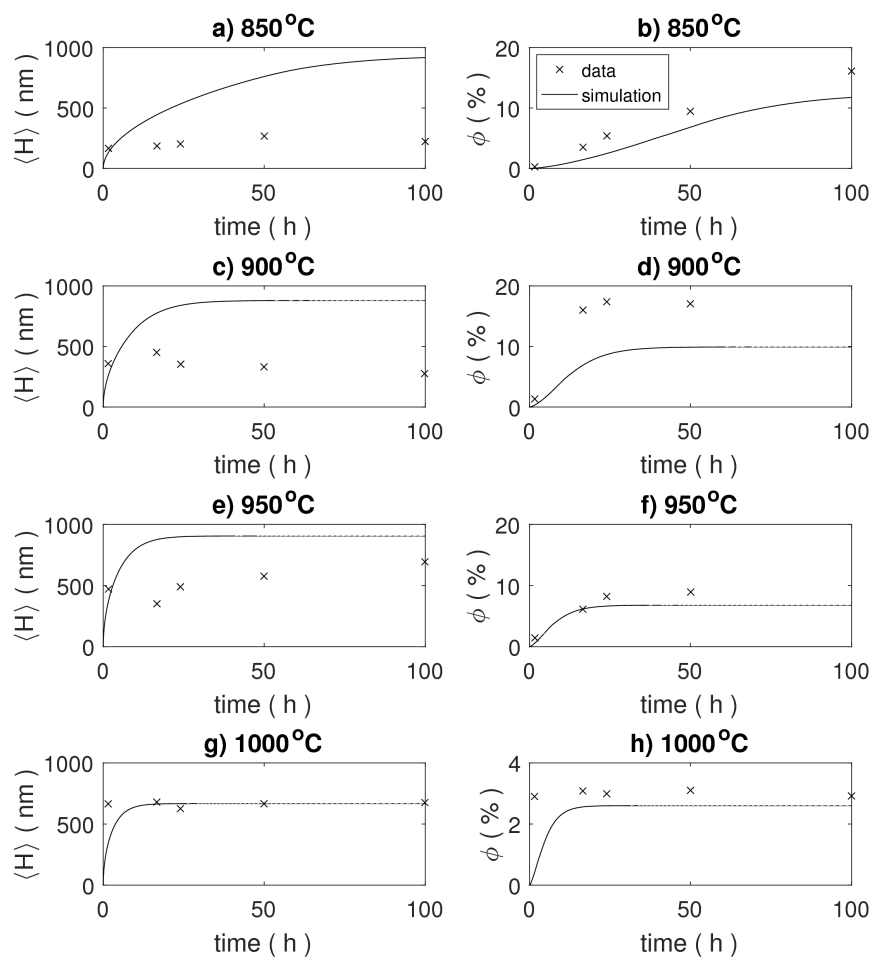


Figure 3: A comparison of predicted δ precipitation kinetics with the measurements of Azadian *et al.* [2], where the left Figures compare the mean particle height of δ particles, $\langle H \rangle$, and the right Figures compares the modelled and measured volume fraction, ϕ .

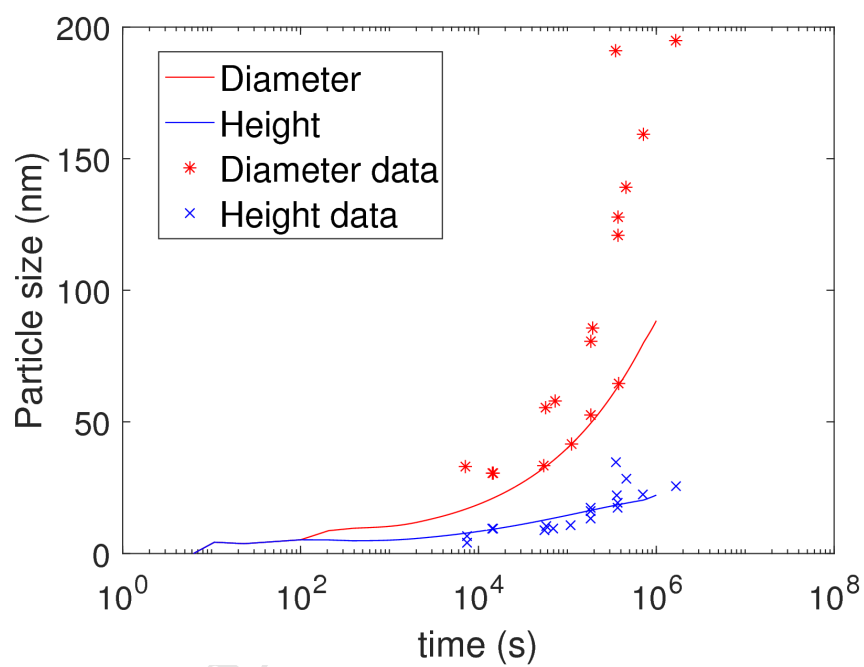


Figure 4: A comparison of predicted γ^* precipitation kinetics with the measurements collated by Fisk *et al.* [1]. The geometry of the γ^* is described by the mean diameter ($\langle D \rangle$) and height ($\langle H \rangle$) of the disc shaped γ^* .

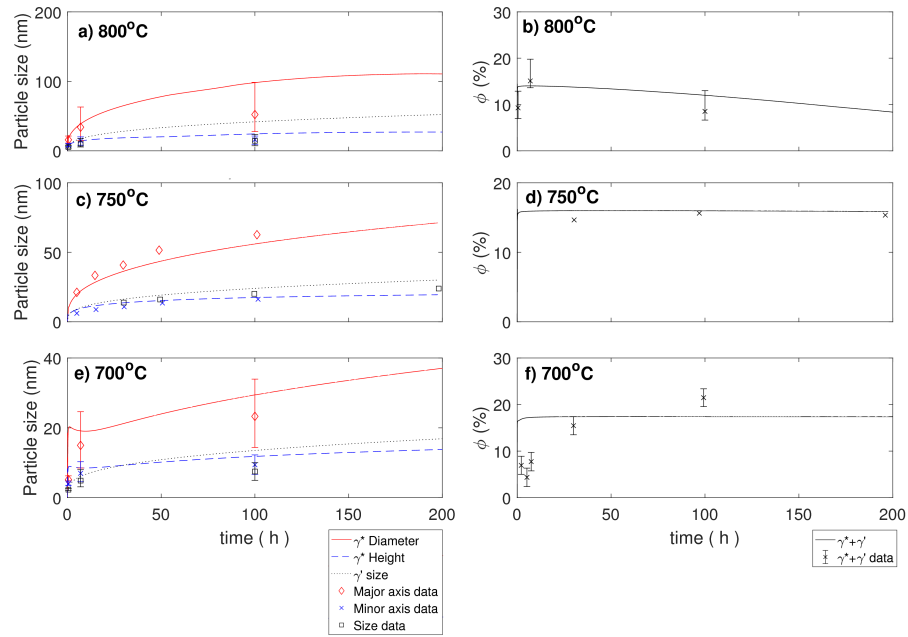


Figure 5: A comparison of predicted γ' and γ^* precipitation kinetics with the measurements of Brooks and Bridges [32] and MaiWald-Immer and Fischersworing-Bunk [31]. Figures a), b) e) and f) compare with measurements taken by Brooks and Bridges [32] and Figures c) and d) compare with measurements taken by MaiWald-Immer and Fischersworing-Bunk [31]. Figures a), c) and e) compare the precipitate sizes whilst Figures b), d) and f) compare precipitate volume fractions.

The parameters used to define the heat source have been calibrated using the computational fluid dynamics described by Panwisawas *et al.* [45, 46] to calculate the thermal fields during deposition. Typical predicted thermal fields for the largest geometry are shown in Figure 7. Figure 7 a) shows the thermal field at the cross section illustrated in Figure 6 b) near the end of the deposition. The temperature history predicted at the four locations identified in Figure a) are shown in Figures b), c) and d). The repetitive passes of the laser cause spikes in temperature. These are compared with the solidus temperature of the matrix phase (T_s), and the solvus temperature of the various intermetallic phases. When the deposition layer is close to the point of interest, the temperature is predicted to exceed the solidus temperature of the matrix phase. The temperature reached in subsequent passes exceeds the solvus temperatures of the intermetallic phases. The next section presents the model predictions for the precipitation kinetics during such thermal loading.

4. Results

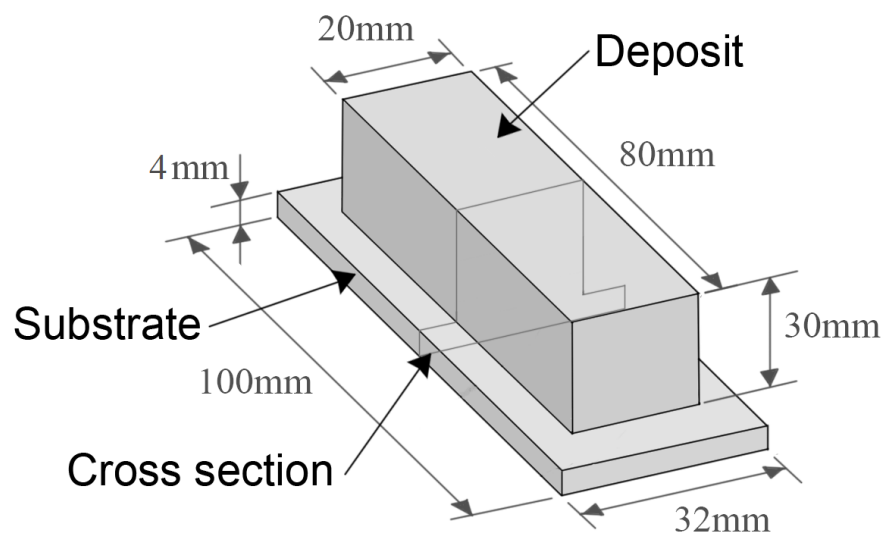
4.1. Heat treatment

The mean-field precipitation model has been developed to assist in the design of heat treatments. Typical heat treatments for this alloy involve a solid-solution treatment for 1 hour at a temperature varying between 930 and 980°C, followed by a fast quench rate and a two step aging process [39]. The aging process lasts 20 hours, with the first 8 hours at 720°C followed by a furnace cool to 620°C.

Figure 8 compares the model predictions to the measurements of MaiWald-Immer and Fischersworrington-Bunk [31] [31], where the first axis shows the heat treatment and the second compares the predicted precipitate size considering γ' and γ^* . The model predictions show reasonable agreement with the experimental data.

The model has been applied to assess different solid solution treatment (SST) temperatures and the cooling rate from solid solution treatment on the predicted

a) Geometry and dimensions



b) Deposition simulation

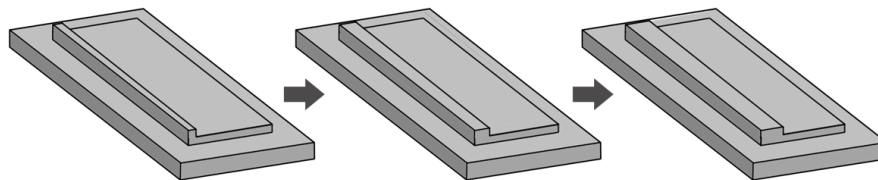


Figure 6: a) The geometry of the AM component and location of the cross section where precipitation kinetics has been evaluated. b) The build sequence used to simulate the AM process.

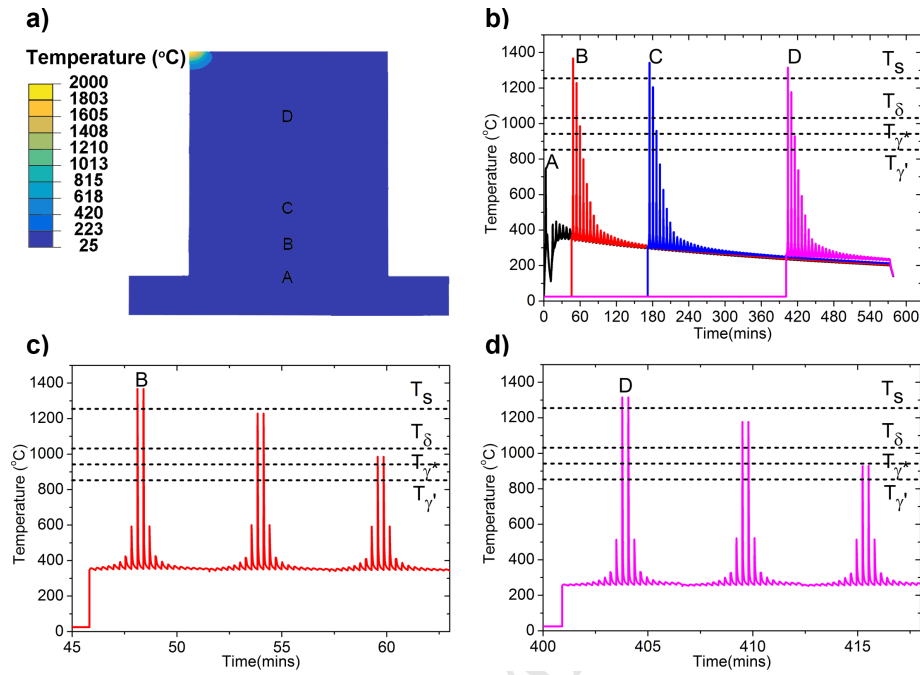


Figure 7: a) The thermal field predicted in the component near the completion of the component build and the location of four points of interest. b) The comparison of predicted thermal history at the four locations illustrated in Figure a). The solvus temperature of all phases of interest are included, where T_s refers to the solidus temperature of the matrix phase. Figures c) and d) show more detail regarding the thermal fields during deposition at locations B and D, respectively.

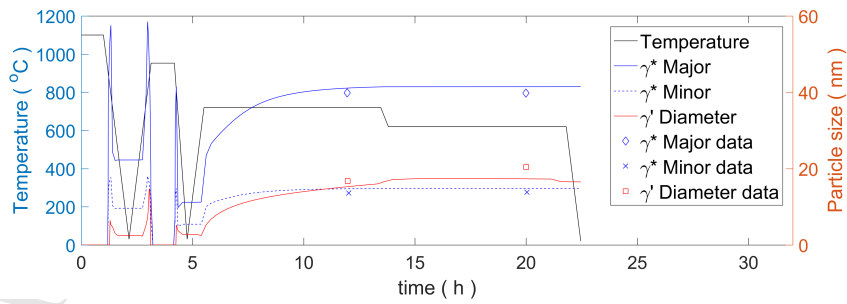


Figure 8: The first axis shows the simulated heat treatment, descriptive of conventional solid solution treatment and aging. The second axis compares the predicted evolution of the size of the γ' and γ^* with the experimental data measured by MaiWald-Immer and Fischersworing-Bunk [31] [31].

multi-phase precipitate dispersions. In addition, simulations have been carried out at temperatures lower than the minimum solid solution treatment temperature typically used for this alloy to explore heat treatments that can obtain a bimodal γ^* particle distribution. Bi-modal particle populations are of interest as they may provide beneficial mechanical properties. The presence of the smaller particle population decreases the mean free path of dislocation glide, and may improve creep life.

The results show that this is possible when performing the SST at a temperature below the γ^* solvus ($\sim 940^\circ\text{C}$) with a fast quench rate. If the quench rate is too slow, the model predictions that the γ^* particles that survive during solid solution treatment are able to grow and absorb all of the γ^* formers, leaving insufficient supersaturation for further nucleation. The predicted γ' , and γ^* distributions for select SST temperatures and quench rates are presented in Figure 9. The particle radius distribution functions are expressed in a volume fraction reformulation where $G(R, t)dR = 4\pi/3R^3F(R, t)dR$. This reformulation is advantageous when viewing multi-modal particle distributions. The predictions also suggest that a bimodal particle distribution of γ' is also possible, and occurs when the quench rate is slow and the SST is performed at temperatures greater than 940°C . The predicted γ^* particles in these microstructures are likely to be too large to offer acceptable precipitate strengthening. When examining the mean particle radius of the largest populations of γ' and γ^* , they follow the same trend where a slower cooling rate allows for more growth, and thus larger particles. In certain conditions, the particles cannot grow fast enough to absorb all the particle forming species, allowing for a supersaturated matrix, and the nucleation of an additional particle population.

Figure 10 shows the predicted volume fraction and mean radius of the first and second populations of γ^* to form as a function of the solid solution treatment temperature and the quench rate. Figure 10 a) shows the SST temperatures and quench rates which result in the bimodal distribution which can be seen when the volume fraction of the first population of γ^* particles is less than 10%. Figure 10 b) clearly shows the conditions which result in a high volume

fraction of the second population of γ^* , forming a bimodal distribution. The rise in volume fraction of the second population is mirrored by a concomitant reduction in volume fraction of the first γ^* population. Figures 10 c) and d) show the corresponding change in mean size of the two populations. For temperatures above the γ^* solvus, only one population of γ^* is predicted to form. For slow cooling rates, the model predicts that it is still possible to obtain a unimodal γ^* dispersion when performing a SST at a temperature below the γ^* solvus. The predictions suggest that the volume fraction of the second γ^* particle population may be maximised by performing the SST at a temperature of $\sim 930^\circ\text{C}$ with a quench rate faster than $\sim 0.4^\circ\text{C/s}$.

The statistics regarding the entire predicted γ' , γ^* and δ particle distributions are shown in Figure 11. The model predicts largest the volume fractions of γ' at fast quench rates, and shows similar behaviour as a function of quench rate when the SST temperature is above 940°C . The mean radius of the γ' phase is complicated by the formation of a bimodal particle distribution for conditions where the cooling rate is slow and the SST temperature is above 940°C , as shown in detail in Figure 9. The hot spots in the volume fraction of γ' shown in Figure 11 a) align with the conditions with the lowest volume fraction of γ^* as shown in Figure 10 b). The γ' precipitation kinetics become sensitive to the SST temperature when the SST temperature drops below the solvus temperature of the γ^* phase. The γ^* differs in that the predicted γ^* dispersions are sensitive to all SST temperatures examined due to the precipitation of δ . This behaviour can be explained by the fact that the γ^* and δ phases share a similar stoichiometry, so the presence of one phase interacts with the kinetics of the other. The γ' phase does not compete for Niobium to such an extent as the other phases, so is unaffected by relatively small amounts of δ which are predicted to form under the conditions examined.

4.2. Precipitation during additive manufacture

Simulations of the precipitation kinetics have been performed at the cross section of the AM component illustrated in Figure 6 a). The AM simulation

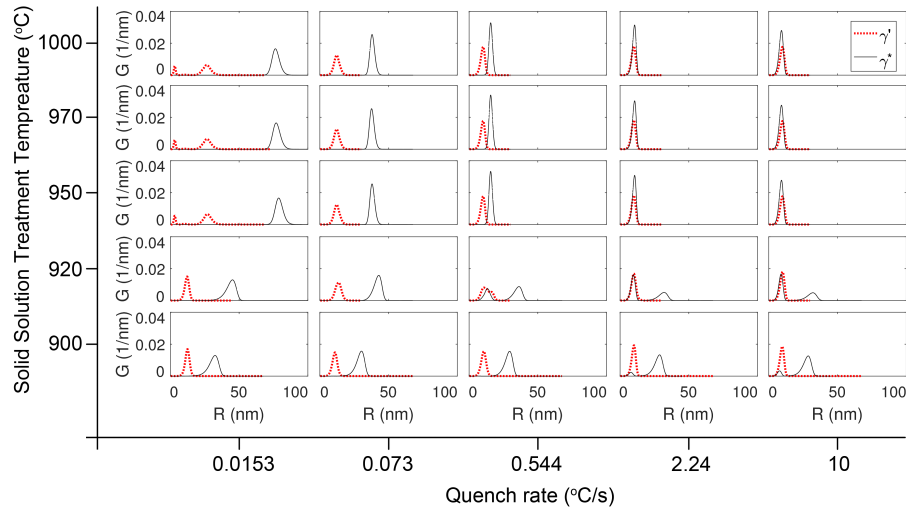


Figure 9: The predicted γ^* and γ' distributions for a range of solid solution treatment temperatures and quench rates. The results show the formation of bimodal precipitate dispersions when the SST is performed below the solvus temperature and at fast quench rates.

follows the build pattern illustrated in Figure 6 b). The substrate is assumed to be Inconel 718, in the heat treated state described in Figure 8. The model is able to capture the repeated precipitation and dissolution of the intermetallic precipitates during additive manufacture, as shown in Figure 12. Figure 12 a) shows the volume fraction of γ' and γ^* predicted at location B in Figure 7 to increase in step changes after passes of the laser. Figure 12 b) shows a close up of the predictions after two passes of the laser. The model predicts the dissolution of the intermetallic phases as the temperature exceeds the solvus temperature of the phases, with re-precipitation upon cooling.

Figure 13 presents predicted distributions in the top, middle and bottom of the deposit at the cross section identified in Figure 6. No precipitation is predicted in the last layer to be deposited. A negligible amount of δ is predicted to form within the rest of the deposit. The γ' and γ^* particles are small, with a mean radius of ~ 1 nm. The predicted volume fraction and precipitate size distributions are larger nearer the bottom of the deposit, which have been exposed to greater thermal loading.

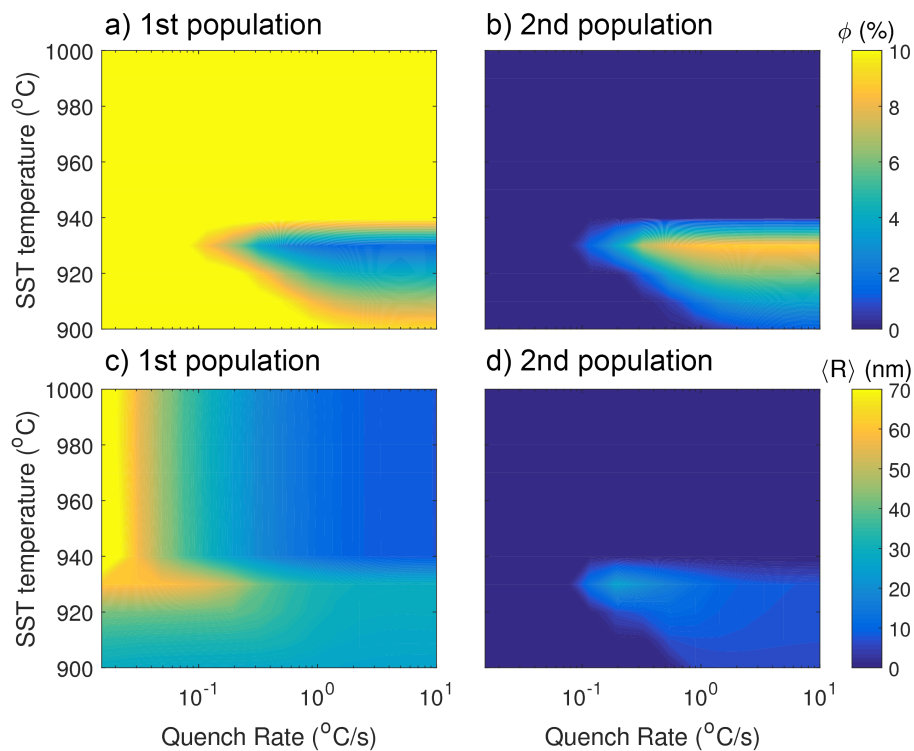


Figure 10: Contour maps showing the mean particle radius and volume fraction of the first and second populations of γ^* as a function of solid-solution treatment temperature and cooling rate. a) The volume fraction of the first population of γ^* present in the dispersion. b) The volume fraction of the second particle, if present. c) The mean particle radius of the first particle population. d) The mean particle radius of the second particle population, if present. Only certain conditions are predicted to result in the formation of a second population of γ^* , which are identified by the hot spot in Figure b).

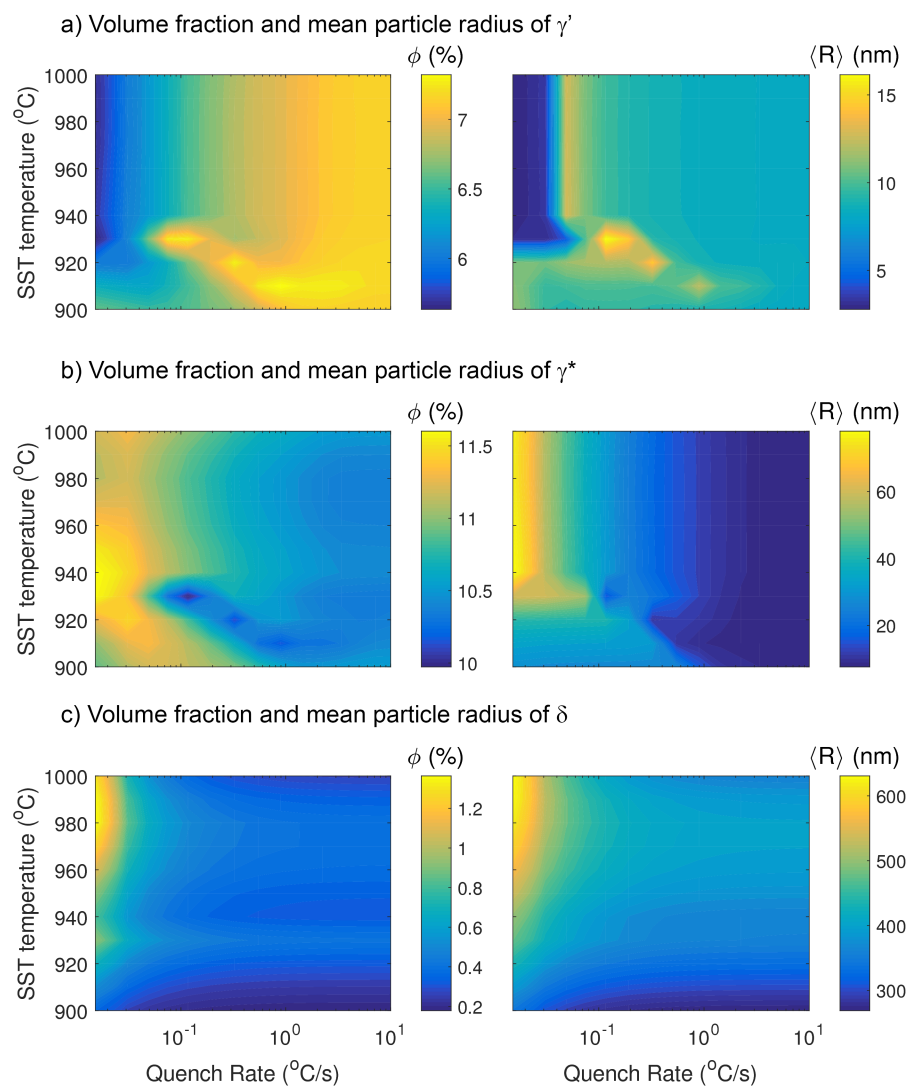


Figure 11: Contour maps showing the volume fraction (left) and mean particle radius (right) of γ' , γ^* and δ as a function of solid-solution treatment temperature and cooling rate.

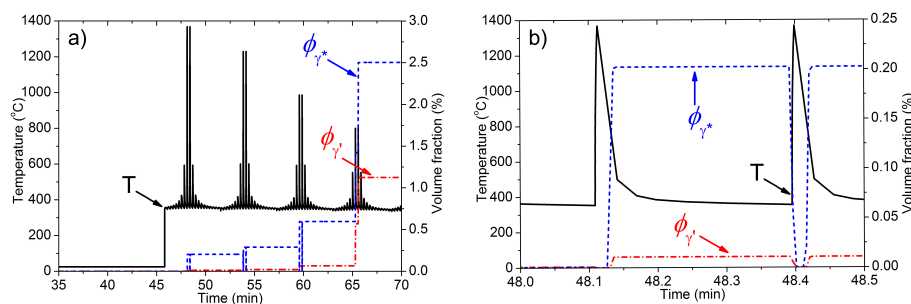


Figure 12: The predicted volume fraction of γ' and γ^* during AM. Figure a) shows the change in volume fraction of γ' and γ^* after multiple layers have been deposited. Figure b) shows the predicted kinetics in greater detail between passes of the laser.

The impact of AM on the substrate may be of interest when repairing a component. The predicted heat affected zone in the substrate is shown in Figure 14. The Figure presents the predicted dispersions at three locations within the substrate; p1: the interface between the deposit and substrate, p2: within the heat-affected zone, and p3: a location deep enough within the substrate for the precipitates to be unaffected by the deposition. The as-heat treated dispersions are observed in the distributions describing p3. At both p1 and p2, the γ' and γ^* dissolve completely and re-precipitate. The model predicts greater nucleation and growth at p1 compared to p2, indicating that p2 is still super-saturated in γ' and γ^* formers. The δ particles are much larger than γ' and γ^* and do not dissolve completely during AM at locations p1 and p2 within the substrate. Instead, they shrink with the largest reduction in size predicted at p1.

5. Discussion

The mean-field model presented in this work offers a useful tool in simulating precipitation kinetics of multiple phases. The simplifying assumptions regarding the geometry and description of the alloying element diffusion fields allows the model to be applied rapidly to different heat treatments. It has been demonstrated that the kinetics of γ' , γ^* and δ can be simulated with reasonable accuracy using the thermodynamic database TTNi8 coupled with the mobility

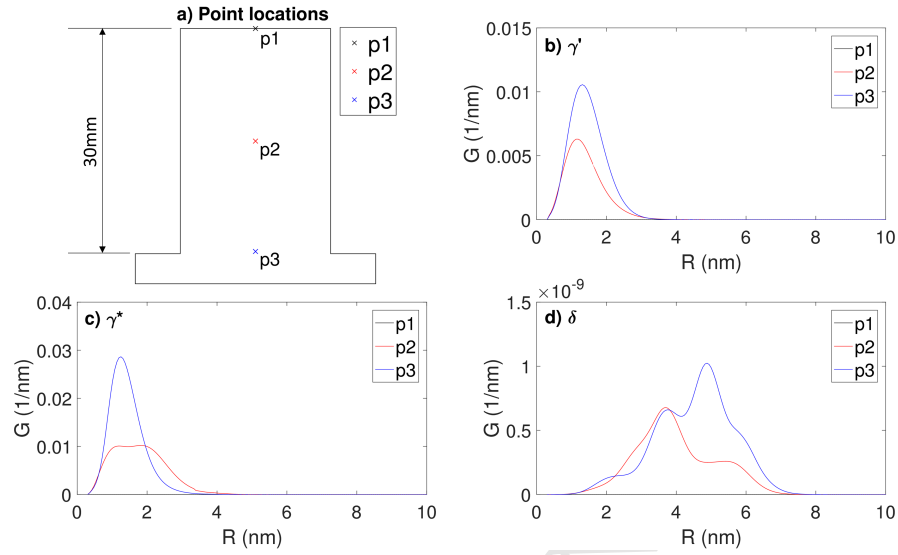


Figure 13: The predicted precipitate dispersions at the top, middle and bottom of the deposit. Figure a) shows the exact locations, whilst Figures b), c) and d) show the predicted distributions for γ' , γ^* and δ , respectively. No precipitation is predicted within the final layer of the deposit at p1.

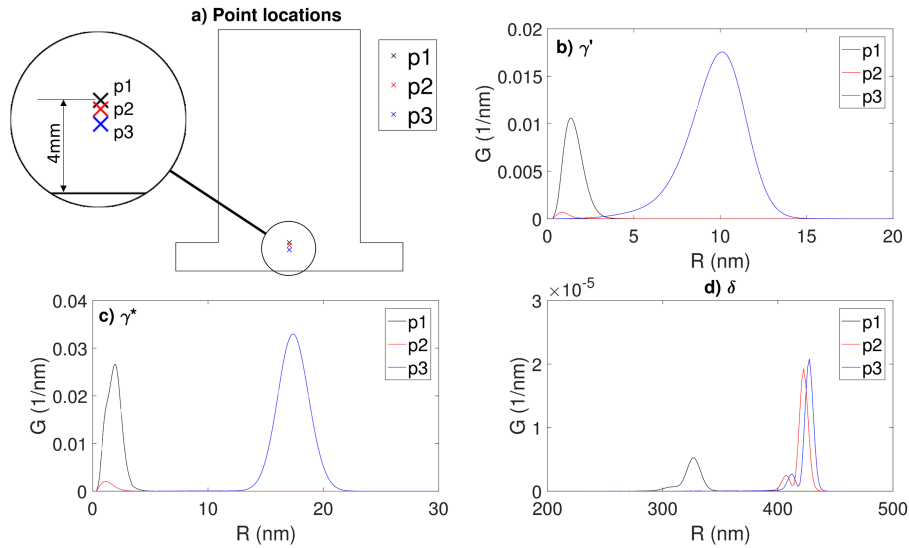


Figure 14: The predicted dispersions within the heat-affected zone of the substrate. Figure a) shows three locations within the substrate. Figures b), c) and d) show the predicted distributions for γ' , γ^* and δ , respectively.

database MOBNI1.

The current model framework utilises the shape factors described by Kozeschnik *et al.* [29], where misfit strain is ignored and the change in the aspect ratio is not accounted for in the growth rate. Svoboda *et al.* [30] have further developed the description of shape factors to describe the evolution of the aspect ratio of the precipitate, account for misfit strain and use a different interfacial energy for the cylinder mantle and top/bottom. They provide a polynomial fit to describe the misfit strain energy as a function of the aspect ratio, elastic moduli, and misfit strain. The derivative of this polynomial with respect to the aspect ratio is used to determine the time derivative of the aspect ratio. Moore *et al.* [28] have adapted this model to describe γ^* in alloy 625, however they used experimental data to determine this relationship. Similar to the method used in this work, Moore *et al.* [28] use experimental data to describe the size-aspect ratio relationship of γ^* .

A description that does not require experimental data would allow the application of the model to new chemistries, taking advantage of the CALPHAD (Computer Coupling of Phase Diagrams and Thermochemistry) nature of the mean-field description of the precipitation kinetics. In Moore *et al.*'s [28] particle growth rate, the change in particle aspect ratio impacts the critical particle radius. The model described in this work may be improved through implementing the description of the shape factors developed by Svoboda *et al.* [30] and Moore *et al.* [28], and applying these improvements to better describe the δ phase in addition to the γ^* phase.

The mean-field model describes Ostwald ripening kinetics with nucleation, however does not account for other phenomena such as particle coalescence or the interaction between the misfit stresses of precipitates. Another consideration is the interaction between γ' and γ^*/δ precipitates, where γ' may impede the growth of γ^* or δ particles as observed by Mignanelli *et al.* [47]. This behaviour may be worth including in alloys with higher volume fractions of γ' to capture more accurately the precipitation kinetics.

The process maps presented in Section 4.1 suggest heat treatments that may

be applied to obtain a bimodal population of γ^* . A bimodal particle population of γ^* may be desirable if the larger population can increase the cutting stress, whilst the smaller particles decrease the mean free path, increasing the Orowan stress for particle bypass. The yield stress models developed by Fisk *et al.* [9], Ahmadi *et al.* [10] and Collins and Stone, [48] consider unimodal particle dispersions, and require further work to capture the details regarding a more complicated multi-modal particle distribution. It can also be argued that these models when applied to Inconel 718 do not account for the combined impact of γ' and γ^* dispersions. Further work is necessary to describe precipitate strengthening arising from a multi-modal particle dispersion and for the case in Inconel 718 where the two dispersions of γ' and γ^* have different shapes.

The application of a mean-field model to predict precipitation kinetics during AM is needed as it allows for the prediction at a component scale. This paper has shown how FEM modelling of AM can be used to generate the thermal histories to simulate using the mean-field precipitation model to offer valuable insights into the understanding of precipitation kinetics during additive manufacture. The model is able to predict the repetitive nucleation and dissolution of particles whilst the heat source is close to the location of interest. The ability to predict the dispersion in the heat-affected zone in the substrate is important when using AM to repair a component without applying a subsequent SST. The precipitation kinetics predicted in the deposit is also of interest, as although the predicted precipitates are small, they may impact stress relaxation behaviour, complicating the component response during any heat treatment aimed at relieving residual stresses.

Makiewicz [49] report similar γ^* and γ' volume fractions in an AM selective melting fabricated component to those predicted in this simulation, however Amato *et al.* [50] have observed larger γ^* precipitates, with a mean equivalent radius of 36nm compared to the 1nm size particles predicted in the geometry studied in this work. The large precipitates observed by Amato *et al.* [50] are surprising, as substantial time at temperature is needed to grow γ^* to reach this size under isothermal conditions [32].

Some differences may be attributed to the different geometries and AM process parameters used in these studies, however there are assumptions made in the application of the model that need further work. The model currently assumes that the chemistry is homogeneous throughout the build, and does not account for the chemical segregation that develops during solidification in the deposit, as measured by Zhang *et al.* [51]. Idell *et al.* [34] also observed dendritic segregation with δ precipitates forming at the Nb rich regions. Kuo *et al.* [52] measured reduced creep-rupture life due to the presence of such δ particles. The current mean-field model is applied to the bulk composition and does not account for such spatial differences in chemistry. The AM component described in this work is built in such a way as to melt a single layer of powder particles in one pass of the laser. Other process parameters or techniques such as Electron Beam melting may melt multiple layers of powder particles, and re-melt more of the previously deposited material. During AM the model indicates that the γ^* and γ' precipitates repeatedly nucleate and dissolve. It is possible that the particle forming species do not fully disperse into the matrix after the dissolution of the γ^* and γ' precipitates. The local variation in particle forming species may accelerate re-precipitation kinetics, allowing for the rapid growth of larger particles. The chemical segregation may impact precipitation kinetics in several ways. More γ^* and δ may precipitate in the Nb rich regions resulting in a spatial variation of precipitates which is difficult to resolve on typical component length scales. The large gradient in chemical concentrations may delay the onset of nucleation as the homogenization of the solute concentration gradients may be energetically preferable than the nucleation of precipitates. The segregation that develops in AM may be increased by the amount of repetitive re-melting. Further work is needed to study the segregation, and account for this behaviour when calculating precipitate kinetics.

6. Conclusions

A multi-component, multi-phase mean-field model has been applied to capture the kinetics of the intermetallic precipitate phases in Inconel 718. The modelling approach has reached a maturity in which industrially relevant problems can be solved, such as assisting in the design of heat treatments. In this work, the process map has helped identify potential heat treatments for obtaining a bimodal γ^* size distribution. The CALPHAD based mean-field model is capable of describing the kinetics of multiple precipitate phases, stable and metastable, within a unified particle growth rate that captures growth, coarsening and dissolution. This is achieved through the chemical driving force appearing in the calculation for the critical particle radius. This ability is needed when modelling AM, where conventional mean-field models would struggle with the repetitive nucleation, growth and dissolution of the particle populations that occur in the deposit. The results demonstrate how mean-field precipitation predictions may be performed at a component level, providing location specific properties. The mean-field modelling assumptions regarding the precipitate and matrix chemistries appear to be suitable when considering conventional heat treatments, however care is needed when applying these assumptions to more complex processes such as AM.

Acknowledgements

We thank the Aerospace Technology Institute (ATI) for funding this work through the Manufacturing Portfolio programme (project number 113084). The computations described in this paper were performed using the University of Birmingham's BlueBEAR HPC service, which provides a High Performance Computing service to the University's research community.

See <http://www.birmingham.ac.uk/bear> for more details. The authors would also like to show gratitude to the Process Modelling Group within Rolls-Royce plc for their support, with a special thanks to Dr Christos Argyrakakis.

References

- [1] M. Fisk, J. Andersson, R. du Rietz, S. Haas, S. Hall, Precipitate evolution in the early stages of ageing in Inconel 718 investigated using small-angle X-ray scattering, *Mat. Sci. Eng. A-Struct.* 612 (2014) 202–207.
- [2] S. Azadian, L. Wei, R. Warren, Delta phase precipitation in Inconel 718, *Mater. Charact.* 53 (1) (2004) 7–16.
- [3] V. Beaubois, J. Huez, S. Coste, O. Brucelle, J. Lacaze, Short term precipitation kinetics of delta phase in strain free Inconel 718 alloy, *Mater. Sci. Tech. Ser.* 20 (8) (2004) 1019–1026.
- [4] N. Zhou, D. C. Lv, H. L. Zhang, D. McAllister, F. Zhang, M. J. Mills, Y. Wang, Computer simulation of phase transformation and plastic deformation in IN718 superalloy: Microstructural evolution during precipitation, *Acta Mater.* 65 (2014) 270–286.
- [5] Y. Desvall, M. Bouzidi, F. Bois, N. Beaudé, Delta phase in inconel 718: Mechanical properties and forging process requirements, in: Loria, EA (Ed.), *Superalloys 718, 625, 706 and various derivatives*, 1994, pp. 281–291.
- [6] M. Dehmas, J. Lacaze, A. Niang, B. Viguière, TEM study of high-temperature precipitation of delta phase in Inconel 718 alloy, *Adv. Mater. Sci. Eng.* (2011) 1–9.
- [7] D. Cai, W. Zhang, P. Nie, W. Liu, M. Yao, Dissolution kinetics of delta phase and its influence on the notch sensitivity of Inconel 718, *Mater. Charact.* 58 (3) (2007) 220–225.
- [8] M. Sundararaman, P. Mukhopadhyay, S. Banerjee, Precipitation of the δ - Ni_3Nb phase in two nickel base superalloys, *Metall. Trans. A* 19 (3) (1988) 453–465.
- [9] M. Fisk, J. C. Ion, L. E. Lindgren, Flow stress model for IN718 accounting for evolution of strengthening precipitates during thermal treatment, *Comp. Mater. Sci.* 82 (2014) 531–539.

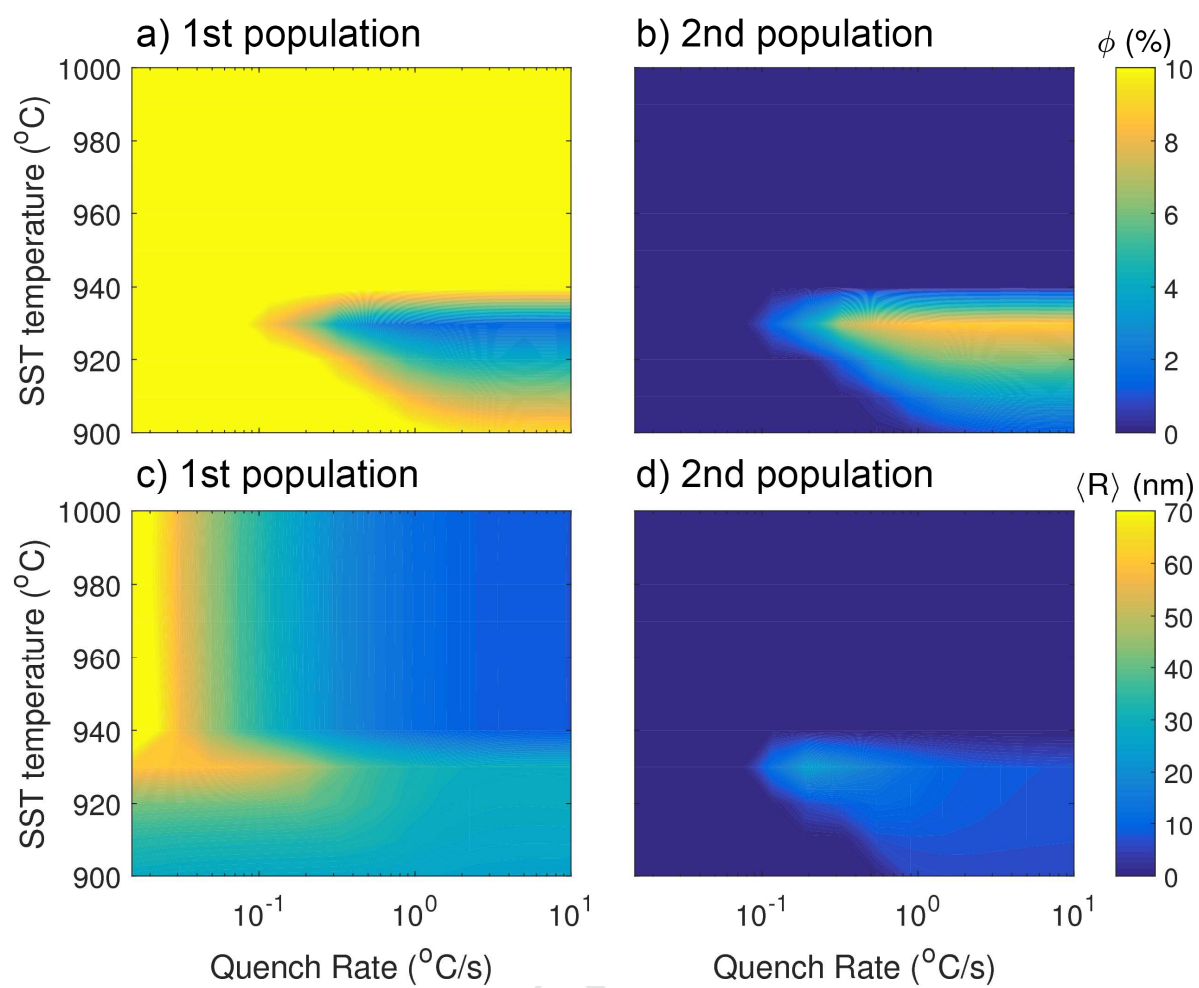
- [10] M. R. Ahmadi, E. Povoden-Karadeniz, L. Whitmore, M. Stockinger, A. Falahati, E. Kozeschnik, Yield strength prediction in Ni-base alloy 718Plus based on thermo-kinetic precipitation simulation, *Mat. Sci. Eng. A-Struct.* 608 (2014) 114–122.
- [11] Z. G. Mao, C. K. Sudbrack, K. E. Yoon, G. Martin, D. N. Seidman, The mechanism of morphogenesis in a phase-separating concentrated multicomponent alloy, *Nat. Mater.* 6 (3) (2007) 210–216.
- [12] E. Clouet, C. Hin, D. Gendt, M. Nastar, F. Soisson, Kinetic Monte Carlo simulations of precipitation, *Adv. Eng. Mater.* 8 (12) (2006) 1210–1214.
- [13] J. Zhu, T. Wang, A. Ardell, S. Zhou, Z. Liu, L. Chen, Three-dimensional phase-field simulations of coarsening kinetics of γ' particles in binary Ni-Al alloys, *Acta Mater.* 52 (9) (2004) 2837–2845.
- [14] R. Duddu, D. L. Chopp, P. Voorhees, B. Moran, Diffusional evolution of precipitates in elastic media using the extended finite element and the level set methods, *J. Comput. Phys* 230 (4) (2011) 1249–1264.
- [15] I. M. Lifshitz, V. V. Slyozov, The kinetics of precipitation from supersaturated solid solutions, *J. Phys. Chem. Solids.* 19 (1961) 35–50.
- [16] C. Z. Wagner, Theorie der Alterung von Niederschlägen durch Umlösen (Ostwald-reifung), *Z. Elektrochem* 65 (1961) 581–591.
- [17] H. J. Jou, P. W. Voorhees, G. B. Olson, Computer simulations for the prediction of microstructure/property variation in aeroturbine disks, in: Green, KA *et. al.* (Ed.), *Superalloys 2004*, (2004), pp. 877–886.
- [18] J. Svoboda, F. D. Fischer, P. Fratzl, E. Kozeschnik, Modelling of kinetics in multi-component multi-phase systems with spherical precipitates: I: Theory, *Mat. Sci. Eng. A-Struct.* 385 (2004) 166–174.
- [19] S. L. Semiatin, S.-L. Kim, F. Zhang, J. S. Tiley, An Investigation of High-Temperature Precipitation in Powder-Metallurgy, Gamma/Gamma-Prime Nickel-Base Superalloys, *Metall. Mater. Trans. A* 46A (4) (2015) 1715–1730.

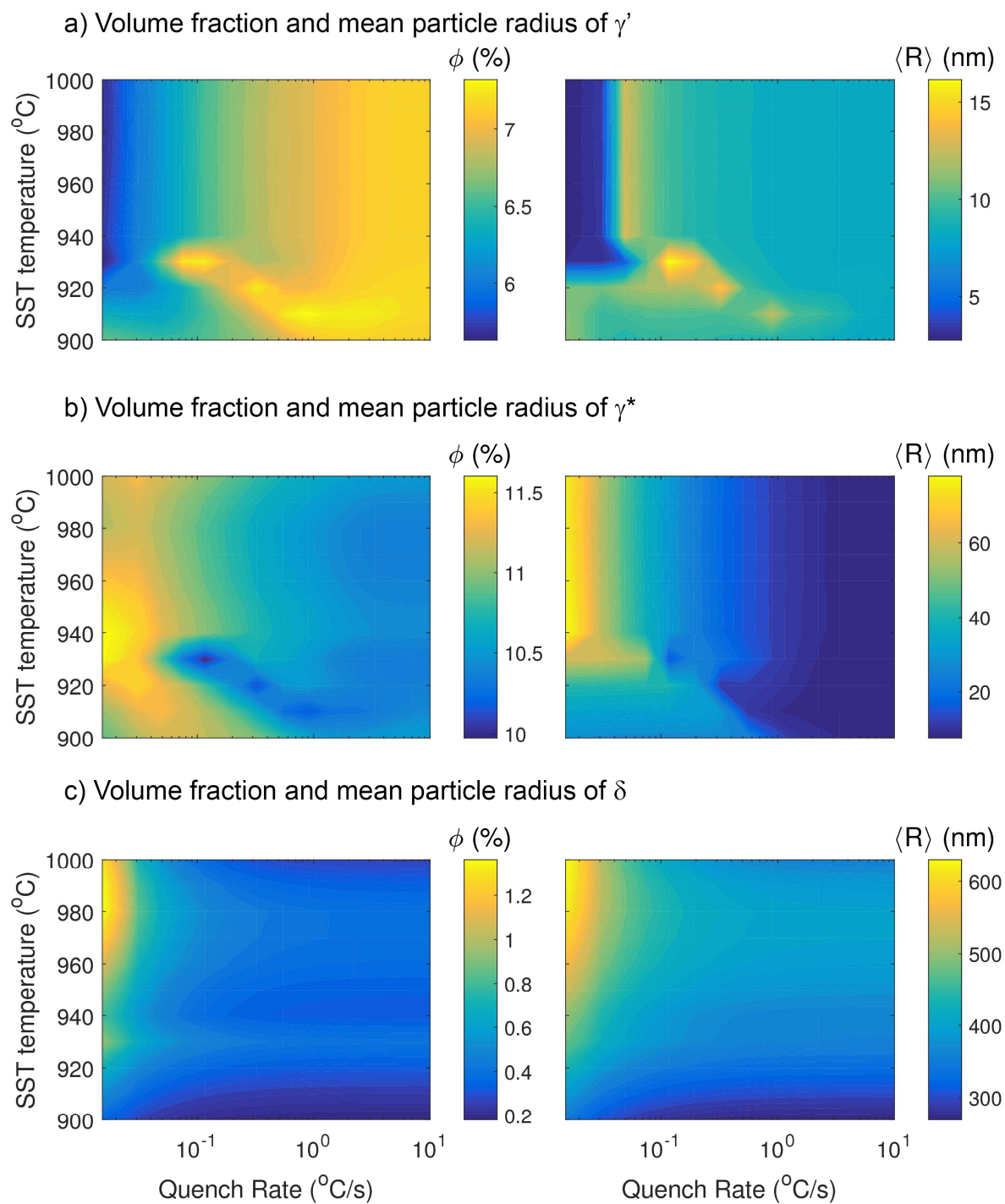
- [20] T. Philippe, P. W. Voorhees, Ostwald ripening in multicomponent alloys, *Acta Mater.* 61 (11) (2013) 4239–4244.
- [21] Q. Chen, J. Jeppsson, J. Agren, Analytical treatment of diffusion during precipitate growth in multicomponent systems, *Acta Mater.* 56 (8) (2008) 1890–1896.
- [22] J. A. Marqusee, J. Ross, Theory of Ostwald ripening - competitive growth and its dependence on volume fraction, *J. Chem. Phys.* 80 (1984) 563–543.
- [23] J. Svoboda, F. Fischer, Generalization of the Lifshitz-Slyozov-Wagner coarsening theory to non dilute multi-component systems, *Acta Mater.* 79 (2014) 304 – 314.
- [24] P. W. Voorhees, M. E. Glicksman, Solution to the multi-particle diffusion problem with applications to Ostwald Ripening. 1. Theory, *Acta Metall. Mater.* 32 (11) (1984) 2001–2011.
- [25] K. G. Wang, M. E. Glicksman, K. Rajan, Length scales in phase coarsening: Theory, simulation, and experiment, *Comp. Mater. Sci.* 34 (3) (2005) 235–253.
- [26] H. Basoalto, M. Anderson, An extension of mean-field coarsening theory to include particle coalescence using nearest-neighbour functions, *Acta Mater.* 117 (2016) 112–134.
- [27] G. A. Zickler, R. Radis, R. Schnitzer, E. Kozeschnik, M. Stockinger, H. Leitner, The precipitation behavior of superalloy ATI Allvac 718Plus, *Adv. Eng. Mater.* 12 (3) (2010) 176–183.
- [28] I. J. Moore, M. G. Burke, E. J. Palmiere, Modelling the nucleation, growth and coarsening kinetics of γ'' ($D0_{22}$) precipitates in the Ni-base Alloy 625, *Acta Mater.* 119 (2016) 157–166.
- [29] E. Kozeschnik, J. Svoboda, F. D. Fischer, Shape factors in modeling of precipitation, *Mat. Sci. Eng. A-Struct.* 441 (1-2) (2006) 68–72.

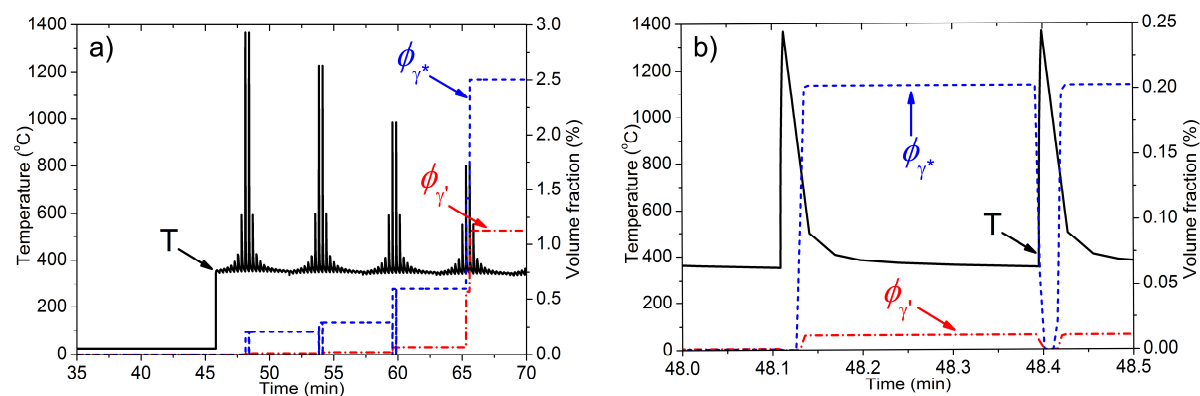
- [30] J. Svoboda, F. D. Fischer, P. H. Mayrhofer, A model for evolution of shape changing precipitates in multicomponent systems, *Acta Mater.* 56 (17) (2008) 4896–4904.
- [31] T. Maiwald-Immer, T. Goehler, A. Fischersworring-Bunk, From melt pool to strength - application of ICME methods for the development of rapid manufacturing technologies, *Proceedings of the 3rd World Congress on Integrated Computational Materials Engineering (ICME)* (2015) 215–220.
- [32] J. W. Brooks, P. J. Bridges, Metallurgical stability of Inconel alloy 718, *Superalloys 1988* (1988) 33–42.
- [33] W. M. Tucho, P. Cuvillier, A. Sjolyst-Kverneland, V. Hansen Microstructure and hardness studies of Inconel 718 manufactured by selective laser melting before and after solution heat treatment, *Mat. Sci. Eng. A-Struct.* 689 (Supplement C) (2017) 220–232.
- [34] Y. Idell, L. E. Levine, A. J. Allen, F. Zhang, C. E. Campbell, G. B. Olson, J. Gong, D. R. Snyder, H. Z. Deutchman, Unexpected δ -phase formation in additive-manufactured Ni-based superalloy, *JOM* 68 (3) (2016) 950–959.
- [35] E. Clouet, Modeling of nucleation processes, *ASM Handbook 22A* (2010) 203–219.
- [36] M. Bonvalet, T. Philippe, X. Sauvage, D. Blavette, Modeling of precipitation kinetics in multicomponent systems: Application to model superalloys, *Acta Mater.* 100 (2015) 169–177.
- [37] T. Mukherjee, W. Zhang, T. DebRoy, An improved prediction of residual stresses and distortion in additive manufacturing, *Comp. Mater. Sci.* 126 (2017) 360–372.
- [38] J. Andersson, T. Helander, L. Hglund, P. F. Shi, B. Sundman, ThermoCalc & DICTRA, computational tools for materials science, *CALPHAD* 26 (2) (2002) 273–312.

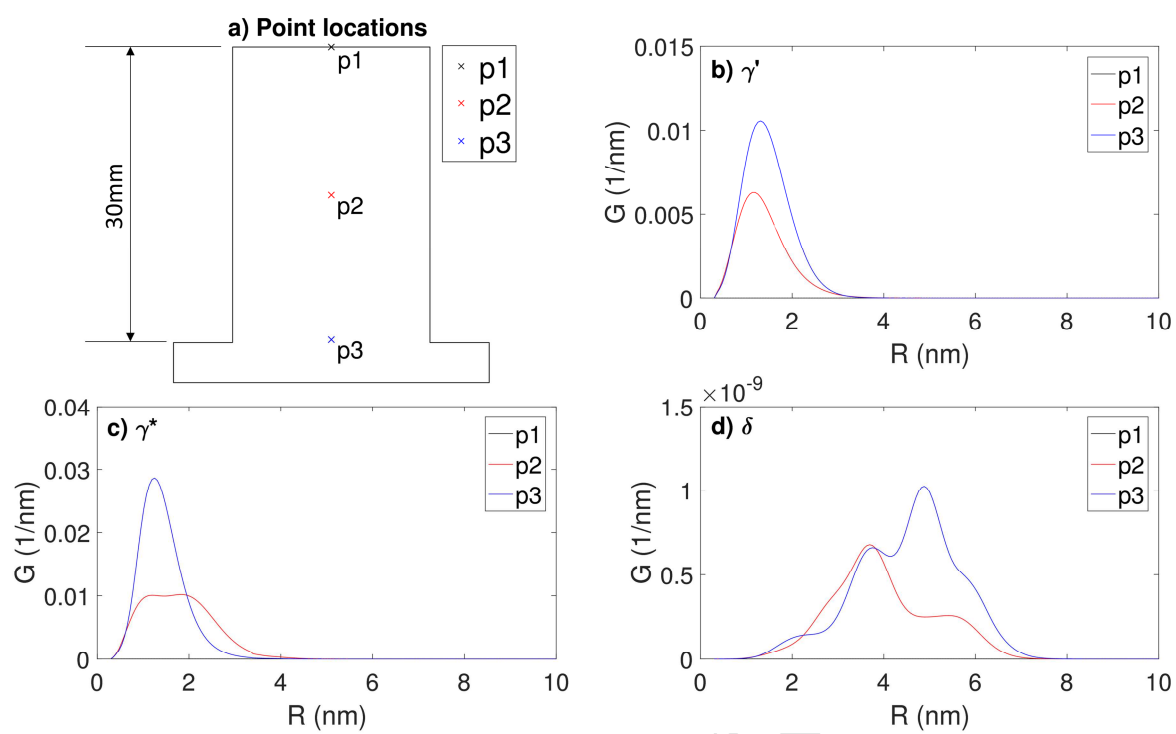
- [39] J. de Jaeger, D. Solas, T. Baudin, O. Fandeur, J.-H. Schmitt, C. Rey, Inconel 718 single and multipass modelling of hot forging, *Superalloys 2012* (2012) 663–672.
- [40] M. J. Anderson, A. Rowe, J. Wells, H. C. Basoalto, Application of a multi-component mean field model to the coarsening behaviour of a nickel-based superalloy, *Acta Mater.* 114 (2016) 80 – 96.
- [41] M. Anderson, A. L. Thielin, F. Bridier, P. Bocher, J. Savoie Aging of the Inconel 718 alloy between 500 and 750 °C, *J. Mater. Res.* 12 (9) (1997) 2298–2316.
- [42] M. Anderson, C. Thielin, G. Cizeron, δ Phase precipitation in Inconel 718 and associated mechanical properties, *Mat. Sci. Eng. A-Struct* (679) (2017) 48-55
- [43] J. Song, A. Dowson, M. Jacobs, J. Brooks, I. Beden, Coupled thermo-mechanical finite-element modelling of hot ring rolling process, *J. Mater. Process. Tech.* 121 (2-3) (2002) 332–340.
- [44] N. Raghavan, R. Dehoff, S. Pannala, S. Simunovic, M. Kirka, J. Turner, N. Carlson, S. S. Babu, Numerical modeling of heat-transfer and the influence of process parameters on tailoring the grain morphology of IN718 in electron beam additive manufacturing, *Acta Mater.* 112 (2016) 303–314.
- [45] C. Panwisawas, C. Qiu, M. J. Anderson, Y. Sovani, R. P. Turner, M. M. Attallah, J. W. Brooks, H. C. Basoalto, Mesoscale modelling of selective laser melting: Thermal fluid dynamics and microstructural evolution, *Comp. Mater. Sci.* 126 (2017) 479–490.
- [46] C. Panwisawas, Y. Sovani, M. J. Anderson, R. P. Turner, N. M. Palumbo, B. C. Saunders, I. Choquet, J. W. Brooks, H. C. Basoalto, multi-scale multi-physics approach to modelling of additive manufacturing in nickel-based superalloys, in: M. Hardy et al. (Eds.), *Superalloys2016*, TMS, Warrendale, PA, 2016, pp. 1021-1030.

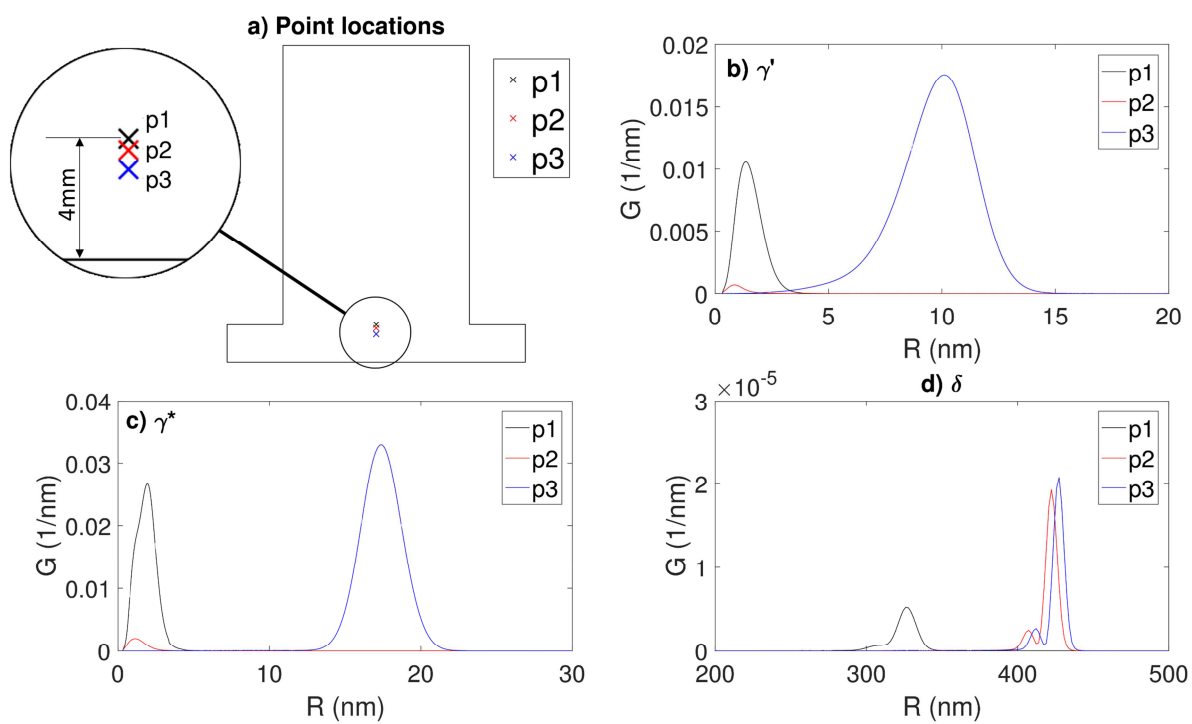
- [47] P. M. Mignanelli, N. G. Jones, E. J. Pickering, O. M. D. M. Messe, C. M. F. Rae, M. C. Hardy, H. J. Stone, Gamma-gamma prime-gamma double prime dual-superlattice superalloys, *Scr. Mater.* 136 (2017) 136–140.
- [48] D. M. Collins, H. J. Stone, A modelling approach to yield strength optimisation in a nickel-base superalloy, *Int. J. Plasticity* 54 (2014) 96–112.
- [49] K. T. Makiewicz, Development of simultaneous transformation kinetics microstructure model with application to laser metal deposited Ti-6Al-4V and alloy 718, Master's thesis, The Ohio State University, Columbus, OH 43210, USA (2013).
- [50] K. N. Amato, S. M. Gaytan, L. E. Murr, E. Martinez, P. W. Shindo, J. Hernandez, S. Collins, F. Medina, Microstructures and mechanical behavior of Inconel 718 fabricated by selective laser melting, *Acta Mater.* 60 (5) (2012) 2229–2239.
- [51] Z. Qun-li, Y. Jian-hua, J. Mazumder, Laser Direct Metal Deposition Technology and Microstructure and Composition Segregation of Inconel 718 Superalloy, *J. Iron. Steel Res. Int.* 18 (4) (2011) 73–78.
- [52] Y.-L. Kuo, S. Horikawa, K. Kakehi, Effects of build direction and heat treatment on creep properties of Ni-base superalloy built up by additive manufacturing, *Scr. Mater.* 129 (2017) 74–78.

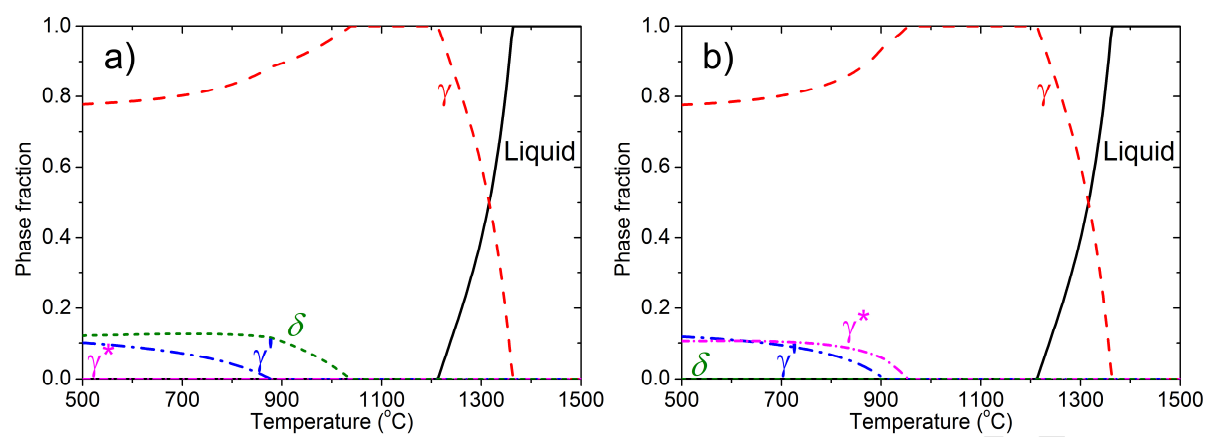


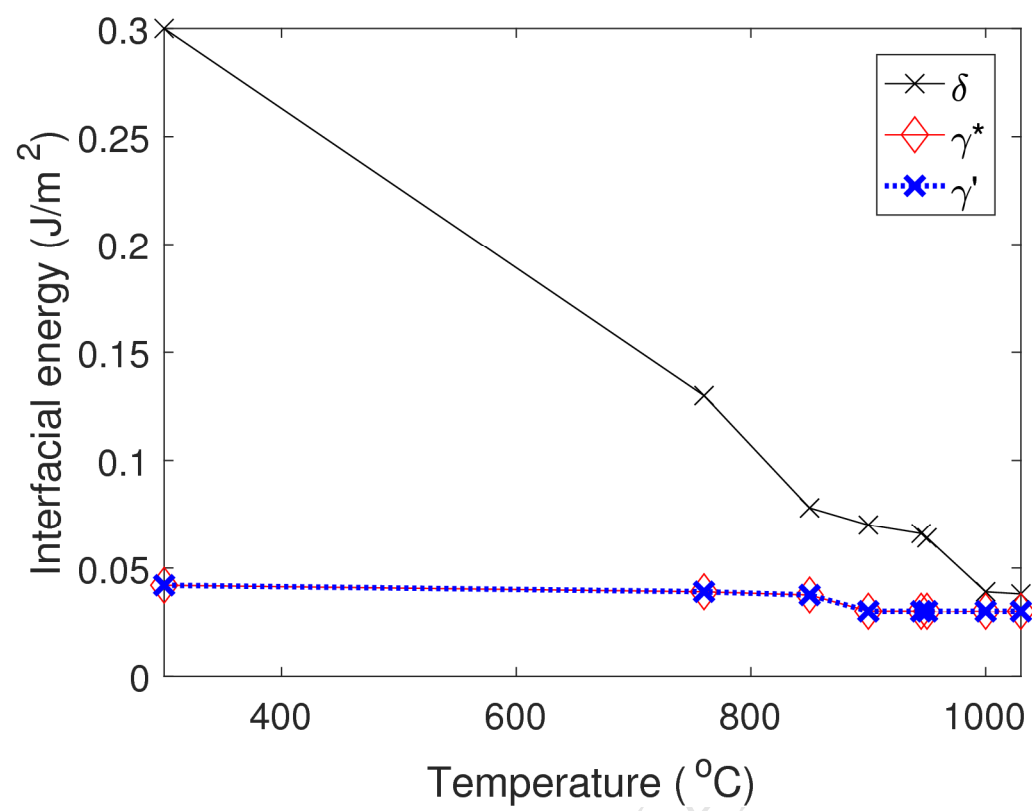


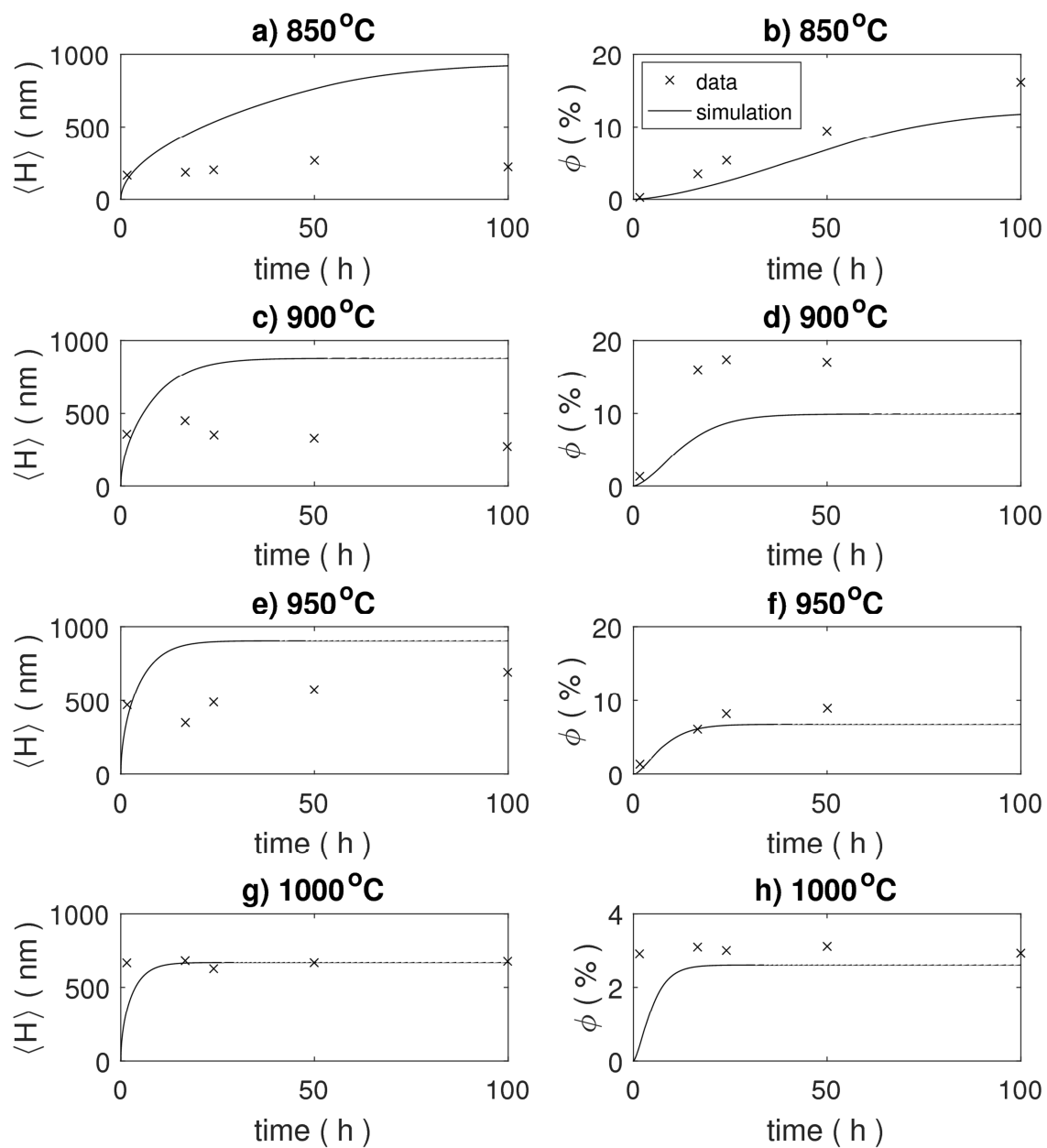


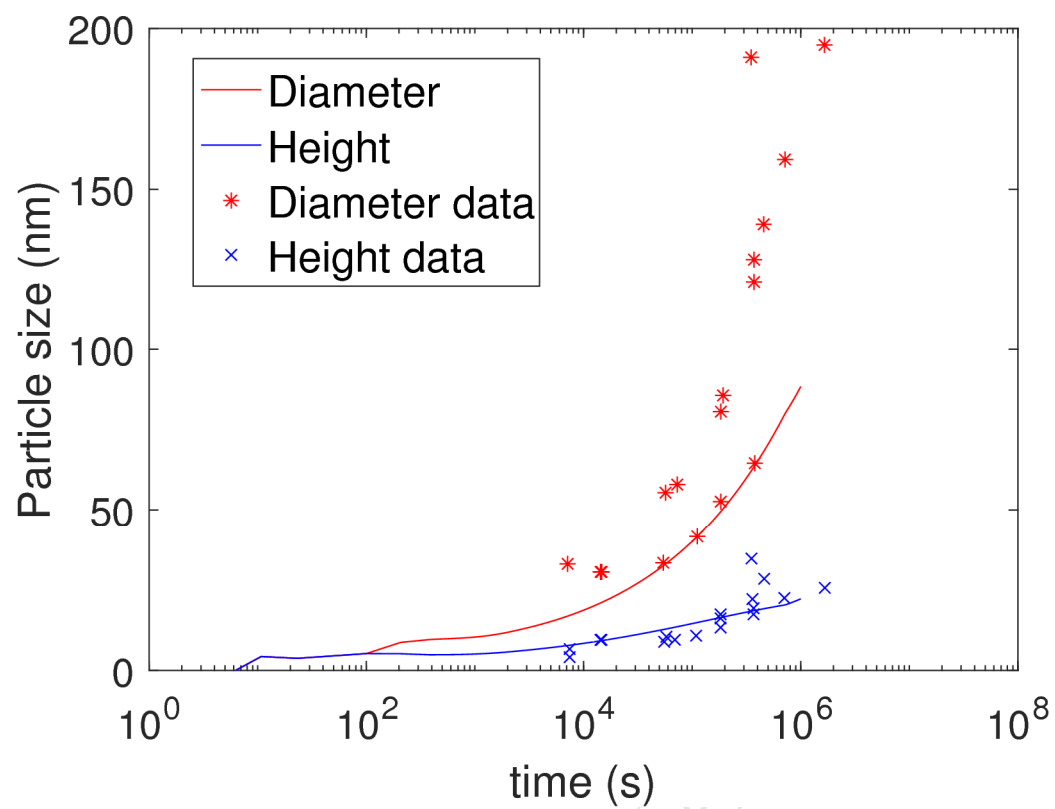


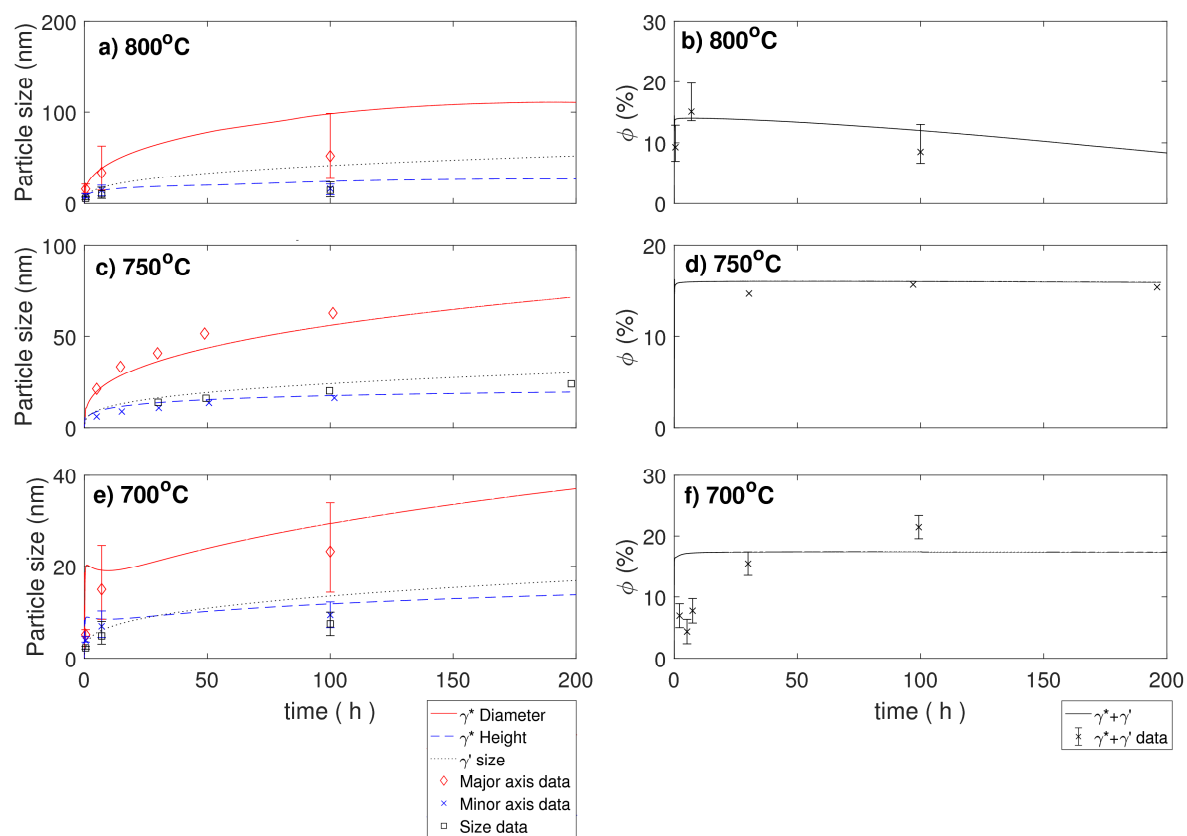




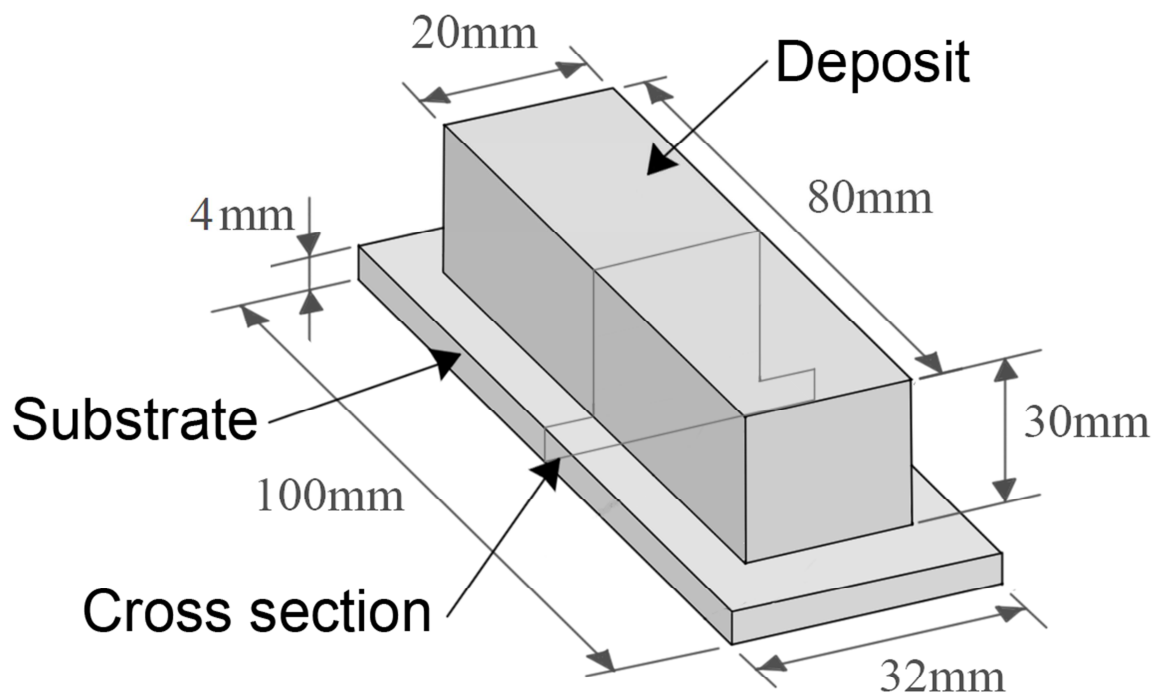








a) Geometry and dimensions



b) Deposition simulation

